

Article

Crystalline Derivatives of Dipyrazolo-1,5-diazocine and Dipyrazolopyrimidine: A Case of Unexpected Synthesis and Isostructural Polymorphism

Fernando Cuenú-Cabezas ^{1,*} , Rodrigo Abonia ²  and Jovanny A. Gómez Castaño ^{3,*} 

¹ Laboratorio de Química Inorgánica y Catálisis, Programa de Química, Universidad del Quindío, Carrera 15, Calle 12 Norte, Armenia 630004, Colombia

² Grupo de Investigación de Compuestos Heterocíclicos, Departamento de Química, Universidad del Valle, Calle 13 No. 100-00, A.A. 25360, Cali 76001, Colombia; rodrigo.abonia@correounivalle.edu.co

³ Grupo Química-Física Molecular y Modelamiento Computacional (QUIMOL[®]), Facultad de Ciencias, Universidad Pedagógica y Tecnológica de Colombia (UPTC), Avenida Central del Norte, Tunja 050030, Colombia

* Correspondence: fercuenu@uniquindio.edu.co (F.C.-C.); jovanny.gomez@uptc.edu.co (J.A.G.C.)

Abstract: Pyrazole-phenylmethanimines (Schiff bases), Py–N=CH–Ph, form molecular crystals whose supramolecular and self-assembly properties can be tuned according to the substitution made on the aromatic and pyrazole rings. In pursuit of the first pyrazole-pyridinemethanimine member, Py–N=CH–Pyr, by following the well-known synthetic scheme for these Schiff bases, two hitherto unknown crystalline derivatives of dipyrazolo-1,5-diazocine and dipyrazolopyrimidine were obtained instead, this depending on the use or not of acetic acid as the catalyst. 1,5-diazocine crystallizes in a single *P*-1 triclinic packing system ($Z = 2$, $Z' = 1$), while dipyrazolopyrimidine exhibits isostructural dimorphic behavior by adopting two (pale pink and yellow) alike $P2_1/c$ monoclinic systems (both $Z = 4$, $Z' = 1$) as a function of the solvent used. Crystal structures were resolved by means of X-ray diffraction technique and their intramolecular, intermolecular, and supramolecular assemblies analyzed with the assistance of decorated Hirshfeld surfaces and the topology study of electron density using the quantum-theory of atoms in molecules (QTAIM). Although both dipyrazolopyrimidine polymorphs are stabilized by the same type of noncovalent motifs, the pale pink crystal has a slightly more compact structure, with more efficient inter- and intramolecular interactions.

Keywords: Schiff bases; polymorphism; 1,5-diazocine; pyrazolopyrimidine; phenylmethanimines



Citation: Cuenú-Cabezas, F.; Abonia, R.; Gómez Castaño, J.A. Crystalline Derivatives of Dipyrazolo-1,5-diazocine and Dipyrazolopyrimidine: A Case of Unexpected Synthesis and Isostructural Polymorphism. *Crystals* **2022**, *12*, 714. <https://doi.org/10.3390/cryst12050714>

Academic Editors: Neil Champness and Younes Hanifehpour

Received: 30 April 2022

Accepted: 14 May 2022

Published: 17 May 2022

Publisher's Note: MDPI stays neutral with regard to jurisdictional claims in published maps and institutional affiliations.



Copyright: © 2022 by the authors. Licensee MDPI, Basel, Switzerland. This article is an open access article distributed under the terms and conditions of the Creative Commons Attribution (CC BY) license (<https://creativecommons.org/licenses/by/4.0/>).

1. Introduction

R-phenylmethanimine derivatives (Schiff bases), with the general structure R–N=CH–Ph, are a versatile class of organic compounds that have evinced multiple applications, for instance, as targets or synthetic-intermediates of active biological ligands [1,2], precursors in organic synthesis [3,4], vanillin derivatives by green chemistry methods [5], oxidized products in the photocatalytic reduction of CO₂ to CH₃OH [6], organic modifying agents to prepare Schiff base-mesoporous silica nanoparticles [7], and other uses [8].

Functionalized pyrazolo-arylmethanimine derivatives **3** form crystalline supramolecular assemblies, stabilized by hydrogen bonds (HBs) and π – π stacking interactions, in which their self-assembly properties and packing geometry can be tuned as a function of the substitutions made in either phenyl or pyrazole rings [9]. Moreover, this type of Schiff base has revealed promising antimicrobial activity [9,10]. Pyrazolo-arylmethanimines **3** can be conveniently synthesized by reacting a substituted-benzaldehyde **1** with a functionalized 5-aminopyrazole derivative **2** in ethanol under mild conditions, as shown in Figure 1.

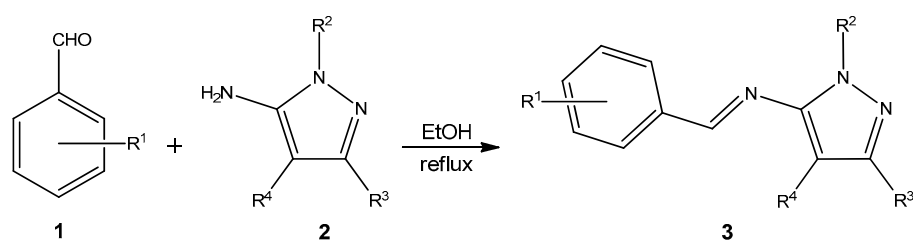


Figure 1. Customary synthesis scheme followed for the preparation of substituted pyrazolo-arylmethanimine derivatives.

In recent years we have been focused on the preparation of novel crystalline pyrazolo-arylmethanimine Schiff bases **3** from hydroxybenzaldehydes ($R^1 = \text{OH}$ in **1**) and 5-amino-3-*tert*-butyl pyrazole **4** in ethanol using acetic acid as the catalyst [11–13]. The molecules in these crystalline packings tend to preserve the co-planarity between the phenol ring and the central $-(\text{H})\text{C}=\text{N}-$ segment, this despite the position of the phenolic hydroxyl and the identity of the R^2 group; whereas their supramolecular architectures were found to range from strong $\pi \cdots \pi$ (between phenol and pyrazole rings) and $\text{C}-\text{H} \cdots \pi$ stacking interactions with absence of HBs (this in the case of the *ortho*-hydroxyl derivative [11]), going through assemblies stabilized by both HBs ($\text{O}-\text{H} \cdots \text{N}$ and $\text{C}-\text{H} \cdots \text{O}$) and $\text{C}-\text{H} \cdots \pi$ interactions, in the case of the *para*-hydroxyl derivative [12], up to strong $\text{O}-\text{H} \cdots \text{N}$ HB interactions only [13].

Continuing our current interest directed toward the structural analysis and synthetic utility of novel 5-aminopyrazole Schiff bases derivatives [10–13], we planned to synthesize the first pyrazolo-pyridinemethanimine derivative **6** as a possible bidentate ligand to be complexed with transition metal ions [14], this as a strategy to produce coordinated compounds **7** that can be evaluated in C–C activation catalytic reactions, as well as potential antifungal and anticancer agents. However, instead of the planned condensation reaction between **4** and 2-pyridinecarboxaldehyde **5** to produce **6**, two different dimerization processes occurred that led to the formation of hitherto unknown derivative solids of 1,5-diazocine **8** and pyrimidine **9**, this depending on the addition or absence of acetic acid, respectively, as the catalyst in the reaction medium (Figure 2).

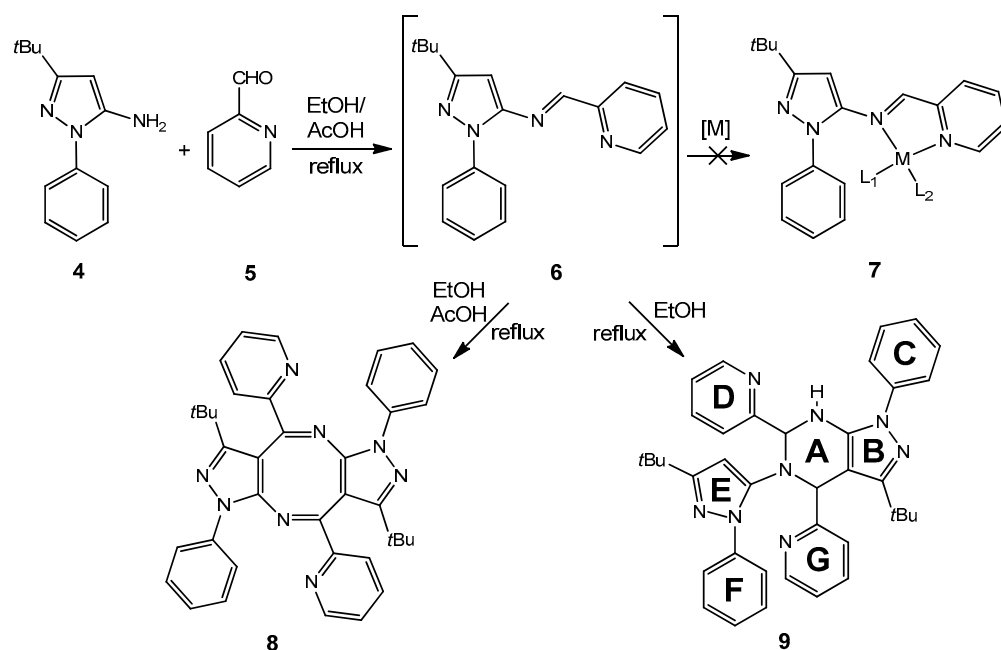


Figure 2. Synthetic scheme to produce novel 1,5-diazocine **8** or pyrimidine **9** derivatives by a dimerization process from 5-amino-3-*tert*-butylpyrazole **4** and 2-pyridinecarboxaldehyde **5**. Capital letter labeling (in bold) in derivative **9** is used for clearer ring sorting.

Single-crystal growth at room temperature of solid **8** led to the formation of a white crystalline structure (space group $P-1$), while crystal growth of solid **9** at room temperature led to the formation of two distinct crystalline polymorphs (dimorphic behavior), a pale pink **9a** and yellow one **9b**, this depending on the solvent used during crystallization. Interestingly, the two pyrimidine polymorphs (**9a** and **9b**) were found to crystallize onto the same space group $P2_1/c$, both with $Z = 4$ and $Z' = 1$ (Table 1), while preserving the same conformational behavior, but exhibiting subtle differences between their cell parameters and supramolecular constructs. Such dimorphic behavior belongs to the denoted isostructural polymorphism [15,16], which is a scarce scenario for the same organic molecular compound and to the best of our knowledge, no other cases are reported for pyrimidine derivatives. The crystalline structures **8**, **9a**, and **9b** were solved using the X-ray diffraction technique, and the analysis of their intramolecular and supramolecular interactions was complemented with the assistance of topological calculations of electron density (ρ) and Hirshfeld surfaces. Additionally, physicochemical and spectroscopic characterization of **8**, **9a**, and **9b** were performed by elemental analysis, GC/MS, FTIR, and (1D and 2D) ^1H -, ^{13}C -NMR.

Table 1. Single crystal X-ray diffraction data and the refinement parameters for compounds **8**, **9a**, and **9b**.

Parameter	8	9a	9b
Empirical formula	$\text{C}_{38}\text{H}_{36}\text{N}_8$	$\text{C}_{38}\text{H}_{40}\text{N}_8$	$\text{C}_{38}\text{H}_{40}\text{N}_8$
Formula weight	604.75	608.78	608.78
Temperature (K)	298(2)	298(2)	298(2)
Wavelength (Å)	0.71073	0.71073	0.71073
Crystal system	Triclinic	Monoclinic	Monoclinic
Space group	$P-1$	$P2_1/c$	$P2_1/c$
a (Å)	11.8094(15)	10.836(4)	10.8383(13)
b (Å)	12.2702(16)	13.346(4)	13.3813(16)
c (Å)	13.9611(18)	23.706(8)	23.732(3)
α (°)	103.307(2)	90	90
β (°)	98.098(2)	100.093(5)	100.068(2)
γ (°)	117.713(2)	90	90
Volume (Å ³)	1669.1(4)	3375.1(19)	3388.9(7)
$Z; Z'$	2; 1	4; 1	4; 1
Calculated density (Mg/m ³)	1.203	1.198	1.193
Absorption coefficient (mm ⁻¹)	0.074	0.073	0.073
$F(000)$	640	1296	1296
Crystal size/shape/color	0.30 mm × 0.20 mm × 0.20 mm/prism/yellow	0.338 mm × 0.238 mm × 0.086 mm/block/colorless	0.25 mm × 0.24 mm × 0.13 mm/prism/yellow
Theta range for data collection	1.57 to 25.38°	1.76 to 25.45°	1.74 to 25.45°
Diffractometer used/Scan Mode	APEX AXS CCD area detector Bruker Smart	APEX AXS CCD area detector	APEX AXS CCD area detector
Index ranges	Omega scans $-14 \leq h \leq 14, -14 \leq k \leq 14, -16 \leq l \leq 16$	Omega scans $-13 \leq h \leq 13, -15 \leq k \leq 16, -28 \leq l \leq 28$	Omega scans $-13 \leq h \leq 13, -16 \leq k \leq 16, -28 \leq l \leq 28$
Reflections collected	13,891	25,186	27,597
Independent reflections	6103 [R(int) = 0.0399]	6173 [R(int) = 0.0778]	6226 [R(int) = 0.0958]
Completeness to theta = 25.38°	99.5%	98.9%	99.4%
Absorption correction	None	Semi-empirical from equivalents	None
Refinement method	Full-matrix least-squares on F^2	Full-matrix least-squares on F^2	Full-matrix least-squares on F^2
Data/restraints/parameters	6103/96/446	6173/54/446	6226/103/449
Goodness-of-fit on F^2	0.896	1.016	0.840
Final R indices [I > 2sigma(I)]	$R_1 = 0.0438, wR_2 = 0.1016$	$R_1 = 0.0592, wR_2 = 0.1341$	$R_1 = 0.0589, wR_2 = 0.1144$
R indices (all data)	$R_1 = 0.0715, wR_2 = 0.1117$	$R_1 = 0.1095, wR_2 = 0.1562$	$R_1 = 0.1578, wR_2 = 0.1380$
Largest diff. peak and hole	0.171 and -0.156 e.Å^{-3}	0.279 and -0.136 e.Å^{-3}	0.514 and -0.126 e.Å^{-3}

2. Materials and Methods

2.1. General Information and Physicochemical Characterization

All chemicals and solvents used (analytical grade) were purchased from Sigma-Aldrich and used without further purification. Melting points were determined on a Büchi melting point apparatus. The mass spectra were obtained on a SHIMADZU-GCMS 2010-DI-2010 spectrometer equipped with a direct input probe operating at 70 eV. Microanalyses were

performed on an Agilent CHNS elemental analyzer and the values were within $\pm 0.4\%$ of the theoretical values. Infrared spectra were measured on a Perkin Elmer FT 2000 series spectrophotometer using KBr disks. The NMR spectra were recorded on a Bruker Avance 400 spectrophotometer operating at 300 MHz for ^1H and at 75 MHz for ^{13}C , using CDCl_3 as the solvent and tetramethyl silane (TMS) as the internal standard.

2.2. Synthesis and Molecular Identification

2.2.1. 3,8-di-tert-butyl-1,6-diphenyl-4,9-di(pyridin-2-yl)-1,6-dihydrodipyrzolo [3,4-b:3',4'-f][1,5]diazocine (8)

Equimolar amounts of the pyrazole precursor **4** (1.350 g, 6.28 mmol) and 2-pyridinecarboxaldehyde **5** (0.679 g, 6.29 mmol) were dissolved in absolute ethanol (6 mL) and refluxed for 24 h in the presence of acetic acid (0.4 mL, 6.80 mmol) as the catalyst. Complete consumption of pyrazole **4** was verified by TLC. After the reaction finished, the formation of a viscous and slightly volatile brown substance was observed. The brown product was dried in a vacuum and dissolved in methanol. The addition of hexane to the methanol mixture led to the formation of a yellow precipitate, which was vacuum filtered and dried at room temperature. No further purification was required.

Yellow solid **8**: 1.669 g (88% yield), m.p. 292.4–293.7 °C, elemental analysis: Exp. %C 75.68; %H 5.96; %N 18.48, cal: %C 75.47; %H 6.00; % N 18.53, for $\text{C}_{19}\text{H}_{18}\text{N}_4$. MS (70 eV) m/z (%) 604 [M^+] (100), [M^+-15] (38.50), [M^+-57] (9.68), [M^+-43] (11.00), [M^+-78] (3.66), [M^+-77] (2.08), 512 (18), 484 (15), 78 (2.24), 77 (3.08), 57 (16.00). FT-IR (KBr, cm^{-1}) $\nu(\text{C-H})$ 3066/3051, $\nu_{\text{sym}}(\text{C-H})$ 2955 (*t*Bu), $\nu_{\text{asym}}(\text{C-H})$ 2866 (*t*Bu), $\nu(\text{C=N})$ 1605, $\nu(\text{C=C})$ 1538/1500. $^1\text{H-NMR}$ (300 MHz, CDCl_3 , δ in ppm) 0.99 (s, 18H, *t*Bu-H), 8.66 (bd, $J = 3.2$ Hz, 2H, Py-H, H-17), 8.09 (d, $J = 8.10$ Hz, 2H, Ph-H, H-14), 7.81 (d, 4H, $J = 7.5$ Hz, Ph-H, H-9), 7.76 (td, 2H, $J = 7.5$ Hz, $J = 2.0$ Hz, Py-H, H-15), 7.41 (t, 4H, $J = 7.5$ Hz, Ph-H, H-10), 7.35 (dd, 2H, $J = 6.5$ Hz, $J = 1.0$ Hz, Py-H, H-16), 7.25 (t, 2H, $J = 7.5$ Hz, Ph-H, H-11). $^{13}\text{C-NMR}$ (75 MHz, CDCl_3 , δ in ppm) 30.19 (*t*Bu- CH_3 , C-7), 33.45 (*t*Bu-Cq, C-6), 105.0 (C-4), 122.1 (C-9), 123.7 (C-14), 125.3 (C-16), 126.1 (C-11), 128.6 (C-10), 136.3 (C-15), 139.4 (C-8), 148.9 (C-3), 149.2 (C-17), 156.9 (C-5), 157.6 (C-13), 170.6 (C=N, C-12). Electron impact fragmentation and FTIR spectra of sample **8** are shown in Figures S1 and S2 (in Supplementary Materials), respectively. ^1H , ^{13}C , and DEPT 1D-NMR spectra in CDCl_3 , as well as atomic numbering used for NMR chemical shift identification, of dipyrzolo-1,5-diazocine derivative **8** are shown in Figures S3–S6.

2.2.2. 3-(tert-Butyl)-5-(3-(tert-butyl)-1-phenyl-1H-pyrazol-5-yl)-1-phenyl-4,6-di(pyridin-2-yl)-4,5,6,7-tetrahydro-1H-pyrazolo[3,4-d]pyrimidine (9)

The reaction conditions to obtain the pyrimidine derivative **9** were the same as those used for the synthesis of compound **8**, except for the addition of acetic acid as a catalyst. Once the reaction was complete, a light pink solid (solid **9a**) was obtained, which was vacuum filtered and washed with a hexane-ethyl ether mixture. The filtrate was allowed to evaporate at room temperature; thus, leaving a yellow solid (solid **9b**), which was purified in a typical column chromatographic separation using a 9:1 hexane dichloromethane ratio and then washed with methanol and ethyl ether.

Light pink solid **9a**: 1.317 g (83% yield), m.p. 255.3–256.8 °C elemental analysis: exp. %C 74.92; %H 6.68; %N 18.39, cal. %C 74.97; %H 6.62; % N 18.41 for $\text{C}_{19}\text{H}_{20}\text{N}_4$. MS (70 eV) m/z (%) 608 [M^+] (27.4), 394 [M^+-214] (100), 338 (22), 70 (14), 57 (13). FT-IR (KBr, cm^{-1}) $\nu(\text{N-H})$ 3275, $\nu(\text{C-H})$ 3070/3055, $\nu_{\text{sym}}(\text{C-H})$ 2958 (*t*-Bu), $\nu_{\text{asym}}(\text{C-H})$ 2862 (*t*Bu), $\nu(\text{C=N})$ 1597, $\nu(\text{C=C})$ 1504. $^1\text{H-NMR}$ (300 MHz, CDCl_3 , δ in ppm) 1.16 (s, 9H, *t*Bu-H), 1.19 (s, 9H, *t*Bu-H), 5.33 (s, 1H), 5.56 (s, 1H), 5.68 (s, 1H), 6.24 (t, 1H, $J = 7.8$ Hz, Py-H), 6.89 (t, 2H, $J = 6.4$ Hz), 7.12–7.14 (m, 3H), 7.26–7.35 (m, 4H), 7.46–7.53 (m, 4H), 7.71 (td, 1H, $J = 7.5$ Hz, $J = 1.2$ Hz, Py-H), 7.89 (d, 2H, $J = 7.0$ Hz), 8.15 (t, 1H, $J = 5.1$ Hz, Py-H), 8.80 (d, 1H, $J = 6.9$ Hz, Py-H). $^{13}\text{C-NMR}$ (75 MHz, CDCl_3 , δ in ppm) 33.57 (*t*Bu-Cq), 32.24 (*t*Bu-Cq), 31.0 (Cq, *t*Bu), 30.32 (*tert*-butyl methyl carbon), 29.87 (*tert*-butyl methyl carbon), 66.5, 66.9, 97.0, 99.7 (Cq), 121.9, 122.7 (Py-C), 122.9 (Py-C), 123.9 (Py-C) 124.2 (Py-C), 125.1, 125.8 (Py-C), 126.0 (Py-

C), 127.9, 129.5, 135.4, 136.3, 139.5 (Py-C), 139.7 (Py-C), 143.7 (Cq), 144.6 (Cq), 147.6 (Cq), 149.8 (Cq), 152.8 (Cq), 158.3 (Cq), 161.2 (Cq), 161.5 (Cq).

Yellow solid **9b**: 1.317 g (83% yield), m.p. 255.1–256.3 °C, elemental analysis: exp. %C 75.03; %H 6.67; %N 18.44, cal. %C 74.97; %H 6.62; %N 18.41 for C₁₉H₂₀N₄. MS (70 eV) *m/z* (%) 608 [M⁺] (26.0), 394 [M⁺-214] (100), 338 (22), 70 (14), 57 (13). FT-IR (cm⁻¹) ν (N-H) 3273, ν (C-H) 3070/3063, $\nu_{\text{sym}}(\text{C-H})$ 2958 (*t*Bu), $\nu_{\text{asym}}(\text{C-H})$ 2864 (*t*Bu), $\nu(\text{C=N})$ 1595, $\nu(\text{C=C})$ 1499. ¹H-NMR (300 MHz, CDCl₃, δ in ppm) 1.15 (s, 9H, *t*Bu-H), 1.17 (s, 9H, *t*Bu-H), 5.33 (s, 1H), 5.56 (s, 1H), 5.68 (s, 1H), 6.24 (t, 1H, *J* = 7.8 Hz, Py-H), 6.89 (t, 2H, *J* = 6.4 Hz), 7.12–7.14 (m, 3H), 7.26–7.35 (m, 4H), 7.46–7.53 (m, 4H), 7.71 (td, 1H, *J* = 7.5 Hz, *J* = 1.2 Hz, Py-H), 7.89 (d, 2H, *J* = 7.0 Hz), 8.15 (t, 1H, *J* = 5.1 Hz, Py-H), 8.80 (d, 1H, *J* = 6.9 Hz, Py-H). ¹³C-NMR (75 MHz, CDCl₃, δ in ppm) 29.9 (*t*-Bu), 30.3 (*t*-Bu), 31.0 (Cq, *t*-Bu), 32.2 (Cq, *t*-Bu), 66.5, 66.9, 97.0, 99.7 (Cq), 121.9, 122.7 (Py-C), 122.9 (Py-C), 123.9 (Py-C) 124.2 (Py-C), 125.1, 125.8 (Py-C), 126.0 (Py-C), 127.9, 129.5, 135.4, 136.3, 139.5 (Py-C), 139.7 (Py-C), 143.7 (Cq), 144.6 (Cq), 147.6 (Cq), 149.8 (Cq), 152.8 (Cq), 158.3 (Cq), 161.2 (Cq), 161.5 (Cq).

Electron impact fragmentation, FTIR, and ¹H and ¹³C 1D-NMR spectra of pyrazolopyrimidine polymorphs are shown in comparative fashion in Figures S7–S9 in Supplementary Materials.

2.3. X-ray Crystal Structure Determination

Single-crystals suitable for X-ray diffraction analysis of solid compounds **8** (yellow), **9a** (light pink), and **9b** (yellow) were grown at room temperature (298 K) by liquid diffusion using a pentane/dichloromethane (precipitant/solvent) system.

Crystallographic data for **8**, **9a**, and **9b** solids were collected at room temperature on a Bruker Apex-II CCD diffractometer using monochromatic graphite MoK α (0.71073 Å) radiation. The determination of their cell and the final cell parameters were obtained on all the reflections using the Bruker SAINT software included in the APEX-2 software package [17]. The integration and scaling of the data were carried out using the Bruker SAINT software [18]. The crystalline structures were solved by direct methods using the Olex2 program [19] and the models obtained were refined by the full-matrix least squares on F₂ (SHELXTL-97) [20]. All the hydrogen atoms were placed in calculated positions and refined with fixed individual displacement parameters [Uiso (H) = 1.2 Ueq or 1.5 Ueq] according to the riding model (C–H bond lengths of 0.93 and 0.96 Å, for methyl and aromatic hydrogen, respectively). Molecular representations were generated by Diamond [21] and MERCURY 3.9 [22] programs. Crystallographic data were deposited at the Cambridge Crystallographic Data Center according to the CCDC reference codes 776,294 (crystal **8**), 776,293 (crystal **9a**), and 776,295 (crystal **9b**).

2.4. Computational Studies

The study of the topology of the electron density (ρ) in the isolated molecules extracted from the unit cells of **8**, **9a**, and **9b** crystals was carried out in the AIM2000 program [23] using wavefunctions calculated in the Gaussian09 program [24] at the theoretical level B3LYP/6-311++g(2df,2pd). This electron topological analysis was performed by applying the Quantum Theory of Atoms in Molecules and Crystals (QTAIM-C) developed by Richard Bader and his coworkers [25]. The calculation of critical points (CPs) on the electron density surface of these molecular systems was performed using Newton's method with a maximum number of 120 iterations and a step-size factor of 0.5. The corresponding molecular graphs were obtained from the calculation of uphill paths from (3, -1) CPs, downhill paths from (3, +1) CPs, and paths connecting (3, -1) and (3, +1) CPs. For each crystalline molecular system, the completeness of the characteristic set of CPs was verified by means of the Poincaré–Hopf relationship ($n_{\text{NCP}} - n_{\text{BCP}} + n_{\text{RCP}} - n_{\text{CCP}} = 1$).

Weak intermolecular interactions between molecules in each crystal structure were studied by using Hirshfeld surface (HS) analysis [26] and the associated two-dimensional fingerprint plots [27] generated using CrystalExplorer21.5 [28]. The three-dimensional d_{norm} surface of the crystal structures **8**, **9a**, and **9b** were generated using a standard surface resolution with a fixed color scale of 0.50–1.70 au (for **8**) or 0.08–1.54 au (for both **9a** and **9b**).

3. Results and Discussion

3.1. 1,5-diazocine Derivative 8

3.1.1. Single-Crystal X-ray Diffraction

The crystallographic parameters of solid the sample **8** are summarized in Table 1. As shown in Figure 3a, its two molecular units ($Z = 2$, $Z' = 1$) are arranged opposite each other around the cell inversion center, forming a cyclic symmetric dimer because of two mutual intermolecular HB connections ($d = 2.785 \text{ \AA}$) between the pyridine nitrogen and the geminal hydrogen of the analogous pyridine ring of the other unit. In turn, each molecular unit is three-dimensionally arranged favoring multiple intramolecular $\text{H}\cdots\text{N}$ distances (in the range of $2.377\text{--}2.665 \text{ \AA}$) and with the 8-membered cycle of the 1,5-diazocine core adopting a bathtub conformational orientation (Figure 3b). Unlike the symmetrical conformational behavior in solution, deduced from NMR spectroscopy (see Section 2.2.2), the 1,5-diazocine molecule **8** in the crystal packing presents variations between geometric parameters of the same functional groups located in opposite positions, which lead to the loss of its axis of symmetry of order 2 (C_2). This perturbation of the molecular symmetry suggests a differential direction of forces in the crystal of compound **8**.

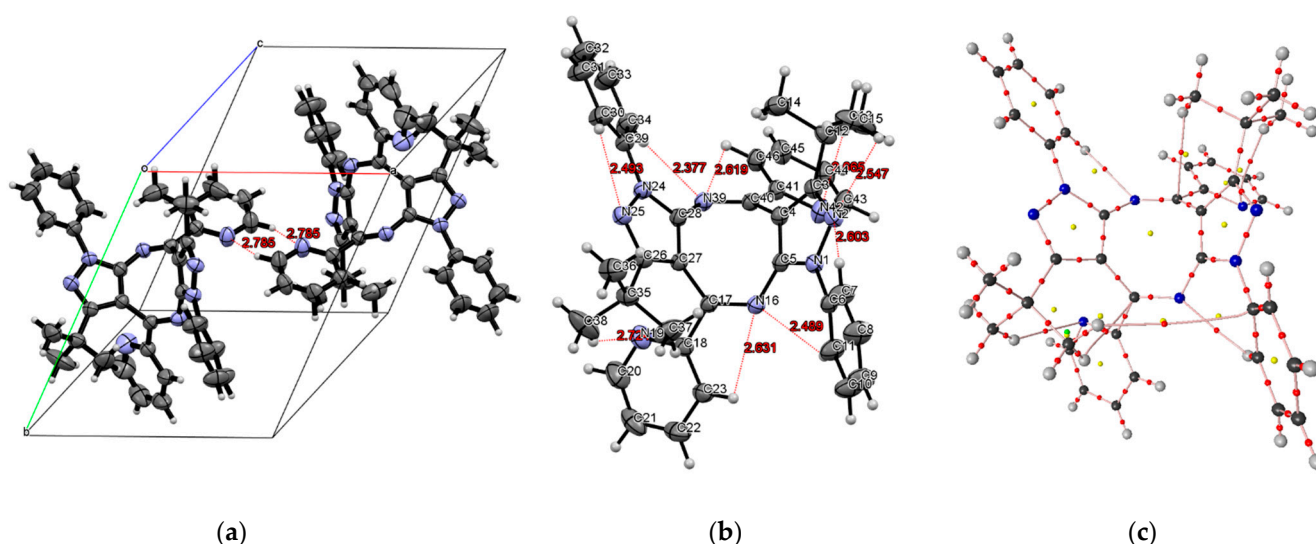


Figure 3. Crystalline structure of 1,5-diazocine derivative **8**. (a) Unit cell containing a symmetric cyclic dimer formed between the two molecular units ($Z = 2$, $Z' = 1$). (b) ORTEP 3D-representation of one molecular unit with the atom numbering. Inter- and intra-molecular HB contacts are presented in dashed red lines with distances (\AA) in red. Displacement ellipsoids are drawn at 50% probability level. (c) Molecular graph for molecular unit showing bond paths (pink lines), BCPs (red dots), RCPs (yellow dots), and CCPs (green dots).

As shown in Figure 4, the two identical molecular units in crystal **8** pack alternatively and with opposite symmetry along the a direction. The nitrogen atom of one of the pyridine rings has two $\text{N}\cdots\text{H}$ hydrogen bonds, one intramolecular and the other intermolecular, both with the same distance (2.724 \AA). The intermolecular $\text{N}\cdots\text{H}$ bond connects to the hydrogen of the carbon in position 3 of the other pyridine ring of the second unit; while the intramolecular $\text{N}\cdots\text{H}$ bond is made with a hydrogen of the *t*Bu group, forming an angle of 96° with respect to the plane of the pyridine ring. The nitrogen atom of the second pyridine ring has an intramolecular HB (2.665 \AA) with a hydrogen of the other *t*Bu group, forming an angle of 89.4° with respect to the pyridine ring. Also shown in Figure 4 is the short (2.377 \AA) intramolecular $\text{N}\cdots\text{H}$ hydrogen bond between a pyrimidine ring nitrogen and an *ortho* hydrogen on one of the phenyl rings. In addition to the $\text{N}\cdots\text{H}$ HBs described above, the packing of crystal **8** features an intermolecular $\text{H}\cdots\text{H}$ interaction (2.241 \AA) between the *t*Bu groups and an intermolecular π -stacking $\text{C}\cdots\text{H}$ interaction (2.812 \AA) between the *ortho*

hydrogen of the phenyl ring and the carbon at the 3-position of the pyridine ring; the latter with an angle of 111.9° with respect to the plane of the pyridine ring.

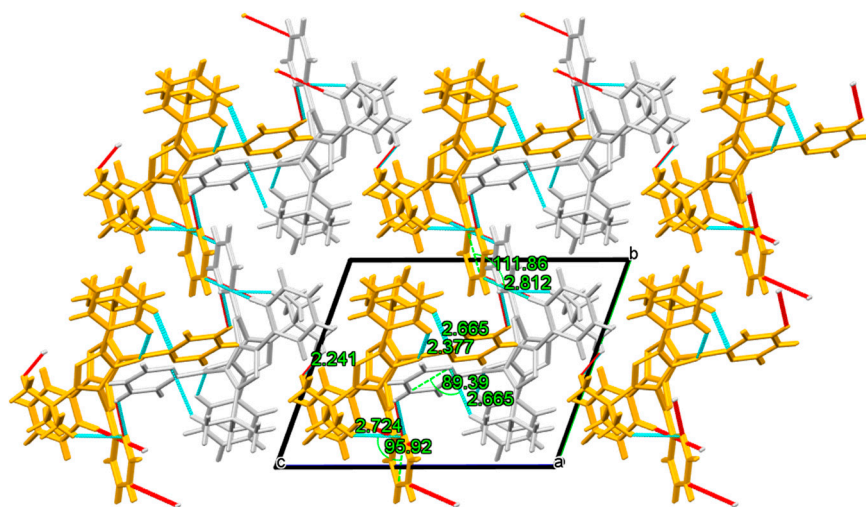


Figure 4. Crystal packing ($2.5 \times 2.5 \times 2.5$ supercell) of 1,5-diazocine **8** seen along the *bc* face and highlighting featured $N \cdots H$ HBs. Molecular units ($Z = 2$, $Z' = 1$) are colored based on different symmetry operations. Intramolecular HBs are shown in cyan, while intermolecular HBs are shown in red. Distances in Angstroms (\AA) and angles in grades ($^\circ$).

3.1.2. Topological Study on Electron Density (ρ)

Theoretical verification and deeper understanding of the intramolecular contacts established in the crystalline molecule of solid **8** comes from the study of the topology of its quantum mechanical (B3LYP/6-311++g(2df,2pd)) electron density by using QTAIM-C [25]. The recovery of all kinds of critical points (CPs) in the ρ gradient field of crystal unit **8** led to the identification of 82 NCPs (3, -3), 95 BCPs (3, -1), 15 RCPs (3, $+1$), and 1 CCPs (3, $+3$), which allows the Pointcaré–Hopf relationship to be fulfilled (n NCPs $- n$ BCPs $+ n$ RCPs $- n$ CCPs = 1); thus demonstrating the completeness of this characteristic set. The corresponding molecular graph showing the CPs along with the calculated bond paths is presented in Figure 3c. As seen when comparing Figure 3b,c, no BCP is recovered between the nonfunctionalized pyrazole nitrogen atoms and the nearest phenyl *ortho* hydrogens, or between the pyrimidine nitrogen N16 and the hydrogen of the pyridine ring attached to C23, thereby neglecting these intramolecular $N \cdots H$ interactions. In contrast, an unexpected $H \cdots C$ closed-shell BCP ($\rho_b = 1.09 \times 10^{-3}$ au, $\varepsilon = 6.52 \times 10^{-1}$ au, $\nabla_{\rho}^2 = 9.34 \times 10^{-4}$ au) is detected, associated with a long-range interaction (bond path = 3.708 \AA) between the aromatic carbon C6 and a hydrogen of the *t*Bu group attached to the furthest pyrazole ring (i.e., $C(6) \cdots H-C(37)$). The presence of this long-range $H \cdots C$ π -stacking contact breaks the symmetry of this molecule; thus preventing the possibility of a proper axis of order 2 (C_2). QTAIM analysis supports the formation of intramolecular π -stacking interactions between pyrimidine carbons C17 or C40 and hydrogens of the nearest *t*Bu groups, as well as the $N \cdots H$ HBs between pyrimidine nitrogen atoms (N16 and N39) and hydrogens in *ortho* position of the nearest corresponding phenyl, and between each pyridine nitrogen (N19 and N42) and a hydrogen of the nearest *t*Bu group. For intramolecular π -stacking $C \cdots H-CH_2$ interactions, both those involving the pyrimidine ring carbons and the long-range one, a very close distance is observed between the respective BCP and the associated RCP, which reveals a low stability of these interactions. A list of the main topological properties of the closed-shell intramolecular BCPs detected in the ρ gradient field of the crystal molecule **8** is presented in Table 2. Particularly for the interactions $C(17) \cdots H-C(37)$ and $N(42) \cdots H-C(15)$, a significantly higher value is observed in their ellipticities (ε) compared to those of the analogous interactions (i.e., $C(40) \cdots H-C(14)$ and $N(42) \cdots H-C(15)$, respectively), denoting a higher π character degree in the former compared to the latter.

Table 2. Topological parameters¹ for closed-shell intramolecular BCPs in crystalline molecular unit **8**. Line separations are included for a better comparison between interactions of the same sort.

Interaction X...Y	Bond Path		$\rho_b(\text{au})$	$\nabla_q^2(\text{au})$	ϵ	$V(r)(\text{au})$	$G(r)(\text{au})$
	$R_X(\text{au})$	$R_Y(\text{au})$					
C(17)...H'-C(37)	2.8870	2.1760	7.932×10^{-3}	7.406×10^{-3}	2.901	4.378×10^{-3}	5.892×10^{-3}
C(40)...H-C(14)	2.8182	2.0915	8.659×10^{-3}	8.012×10^{-3}	1.658	4.806×10^{-3}	6.409×10^{-3}
N(16)...H-C(11)	2.7445	1.9847	1.156×10^{-2}	1.085×10^{-2}	3.847×10^{-1}	6.829×10^{-3}	8.837×10^{-3}
N(39)...H-C(34)	2.6645	1.8363	1.376×10^{-2}	1.308×10^{-2}	2.255×10^{-1}	8.251×10^{-3}	1.067×10^{-2}
N(19)...H-C(38)	3.0277	2.1216	3.346×10^{-3}	5.159×10^{-3}	7.899×10^{-2}	3.294×10^{-3}	4.226×10^{-3}
N(42)...H-C(15)	3.0092	2.0551	7.743×10^{-3}	6.493×10^{-3}	9.354×10^{-1}	4.118×10^{-3}	5.305×10^{-3}
C(6)...H-C(37)	4.0314	2.9757	1.090×10^{-3}	9.337×10^{-4}	6.524×10^{-1}	4.085×10^{-4}	6.711×10^{-4}

¹ Definitions: electron density (ρ_b), Laplacian of electron density (∇_q^2), ellipticity (ϵ), Virial field function ($V(r)$), Lagrangian kinetic energy ($G(r)$).

3.1.3. Hirshfeld Surface Analysis

The Hirshfeld surface (HS) of a molecule of compound **8** in crystal packing, mapped by normalized intermolecular contact distance (d_{norm}), is presented in Figure 5a. Color notations as red, blue, and white are used in d_{norm} Hirshfeld surfaces to indicate intermolecular interactions between vicinal molecules in the crystal, where red zones indicate contacts shorter than van der Waals radii, white zones indicate intermolecular distances equivalent to van der Waals contacts, and blue regions define contacts longer than van der Waals radii [28]. The darkest red spots ($d_{norm} < \text{vdW contact}$) in Figure 5a show the zones of the strongest HB interactions occurring through HS, in this case corresponding to: (i) one reciprocal intermolecular H...H interaction ($d = 1.984 \text{ \AA}$) between *t*Bu hydrogens, (ii) an H...H interaction ($d = 2.052 \text{ \AA}$, described above) between other hydrogens belonging to the same *t*Bu groups involved in the previous H...H interaction (i.e., interaction i), and (iii) reciprocal π -stacking C...H interactions ($d = 2.699 \text{ \AA}$) between the *ortho* hydrogen on the phenyl ring of one unit and the carbon *meta* to nitrogen on the pyridine of the second unit. No red mark is observed in this HS, but white, for the reciprocal HB ($d = 2.785 \text{ \AA}$) that binds the symmetric dimer centered on the unit cell, as presented in Figure 3a, neither are red marks found in the HS for any N...H interactions shown in Figure 4. Next to the d_{norm} HS included in Figure 5, HS mapped over curvedness (C) and over shape-index (S) are presented in Figure 5b,c, respectively. The blue color in Figure 5b indicates the areas of sharp curvature (high curvedness), which are the zones that tend to divide the HS surface into contact patches with each neighboring molecule. While in Figure 5c blue is associated with bump zones ($S > 1$) and red zones with hollows ($S < 1$) in HS.

The 2D-fingerprint plots depicting the distribution and frequency of all intermolecular interactions occurring across the molecular HS in crystal **8** are presented in Figure 6. In these FP plots, H...H interactions prevail throughout the HS area, contributing with a relative frequency of 65%. The greatest contribution to the H...H contacts (in \AA) is obtained for the pairs of distances (d_e, d_i) contained within the quadrant (1.2, 1.2), (2.2, 2.0), (2.1, 1.4), (1.3, 1.8), see the diamond in yellow, with a more pronounced concentration along the diagonal (1.2, 1.2) to (2.2, 2.0). The shorter symmetric H...H distances in this quadrant, i.e., (1.2, 1.2), correspond to interactions between aromatic hydrogens, while the longer nonsymmetric distances (2.2, 2.0) are related to interactions between *t*Bu hydrogens. The small peak centered at $d_e = d_i \cong 1.0 \text{ \AA}$ corresponds to an H...H interaction type ($d = 2.052 \text{ \AA}$) between *t*Bu groups (interaction ii marked as red dots in HS), while the two small peaks at $d_e \cong 1.2$ and $d_i = 0.8 \text{ \AA}$ or $d_e \cong 0.8$ and $d_i = 1.2 \text{ \AA}$ correspond to the reciprocal H...H interactions (interaction i) marked as red dots on the HS (Figure 5a). C...H contacts are the second contributing intermolecular interactions with about 20% of the total HS area and distributed as 11.6% and 8.5% for interactions starting at hydrogen atoms outside and inside the HS, respectively. Most of the C...H area is concentrated over sandwiched pyrimidine

rings because of reciprocal C···H π stacking interactions. The short spikes located at d_e or $d_i \cong 1.6$ Å in the decomposed FP plots for C···H interactions correspond to the π -stacking interactions between the phenyl and pyridine rings marked as red dots in HS (Figure 5a). N···H interactions account for about 13% of the total HS area, with decomposed contributions of 7.0% and 6.2% for acceptor ($d_e < d_i$) and donor ($d_e > d_i$) hydrogen bonds, respectively. In these decomposed FP plots, the short peaks at d_e or $d_i \cong 1.5$ Å are associated with the reciprocal N···H interactions shown in Figure 3a. The C···C contacts account for 1.3% of the total interactions that occur through HS and are mainly associated with reciprocal π -stacking interactions between the carbon atoms of the phenyl ring and the pyridine ring. The tiniest contribution to intermolecular interactions comes from the C···N/N···C contacts, which provide only 0.6% of the area of the HS.

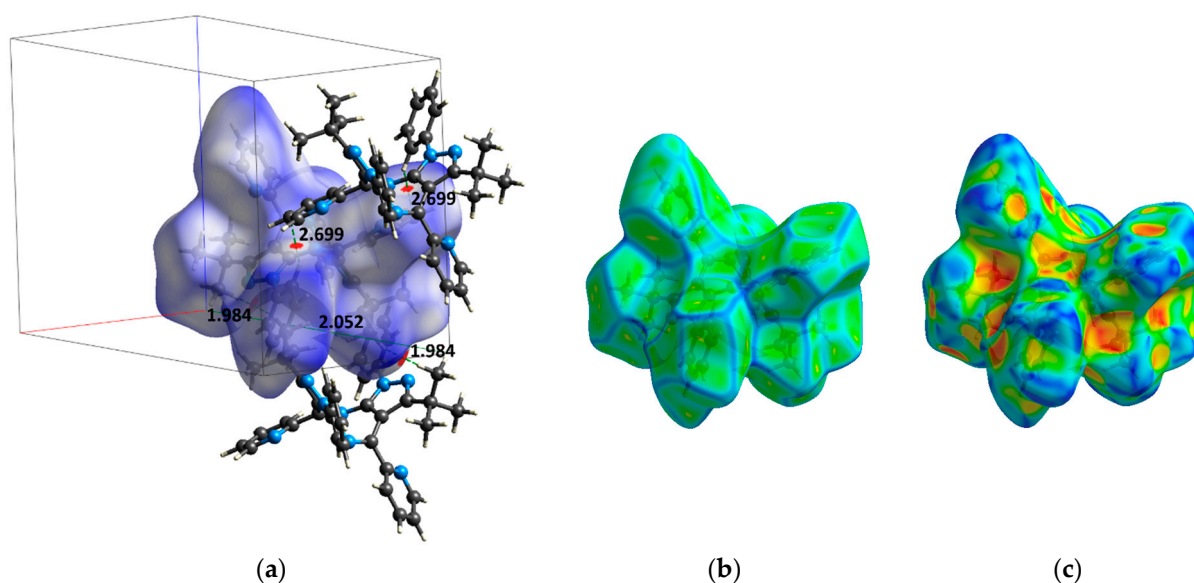


Figure 5. Hirshfeld surface (HS) of a crystal **8** molecule mapped over (a) the normalized contact distance (d_{norm}) scaled over the range 0.5–1.7, (b) curvedness (C) scaled over the range -4.0 – 0.4 , and (c) shape index (S) scaled over the range -1.0 – 1.0 .

3.2. Pyrimidine Derivative **9**

3.2.1. Single-Crystal X-ray Diffraction

As shown in Figure 5, both polymorphs (**9a** and **9b**) crystallized in a monoclinic system (space group $P2_1/c$) with four molecular units per cell ($Z = 4$), with slight differences between their geometric cell parameters (Table 1). From these parameters, a cell similarity index (Π) of 0.0016 and a mean elongation descriptor (ϵ) of 0.0014 were calculated between **9a** and **9b** crystals via Equations (1) and (2), as suggested by Kalman et al. [29,30]. The closer the value of Π and ϵ is to zero each, the more similarity there will be between the matched crystal cells.

$$\Pi = |a + b + c/a' + b' + c'| - 1, \quad (1)$$

where a , b , c and a' , b' , c' are the orthogonalized lattice parameters of the related crystals and satisfy the condition $(a + b + c) > (a' + b' + c')$.

$$\epsilon = (V'/V)^{1/3} - 1, \quad (2)$$

where V and V' are the volumes of the respective unit cells.

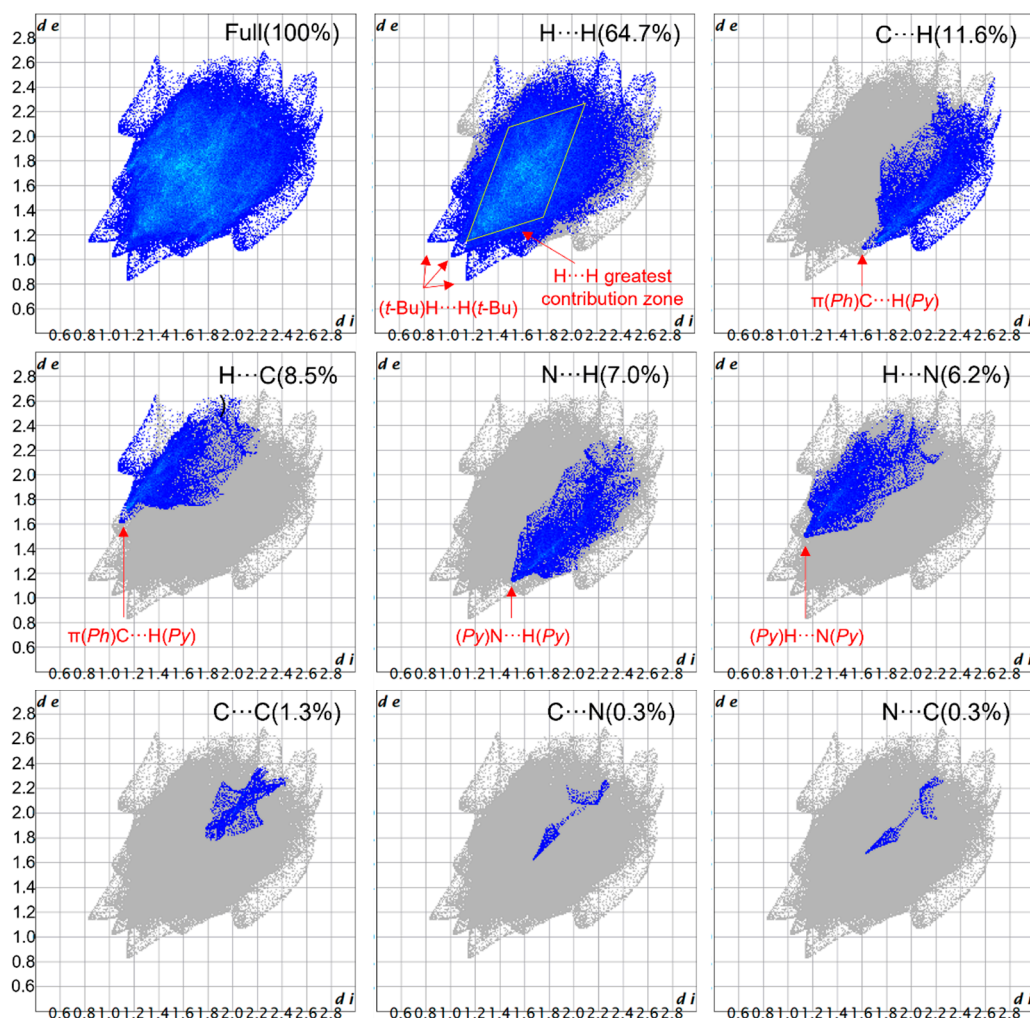


Figure 6. The 2D-fingerprint plots for all and outlined in H···H, C···H, H···C, N···H, H···N, C···C, C···N, and N···C intermolecular contacts through molecular HS in crystal 8. In these A···B contacts, atom A is inside HS, while atom B is outside HS.

Comparison of atomic positions between crystals **9a** and **9b** using CrystalCMP software [31] allowed the estimation of a root mean square deviation (RMSD) of similarity of only 0.024, as depicted by the crystalline overlay plot included in Figure 7.

In **9a** crystal (Figure 7, left), two molecular units are packed antiparallel at the center of the unit cell with two phenyl rings facing each other in a slip fashion (distances: C···C = 3.565, and C···H = 3.172 and 3.262 Å). Furthermore, two identical intermolecular N···H distances of 3.071 Å are found between the nitrogen of a pyridine ring of one unit and the hydrogen in the *para* position of the slipped phenyl ring of the second molecular unit, which can be correlated with a weak-to-moderated HB mutual interaction. The other two molecular units in **9a** are located diametrically opposite each other at two cell vertices. Each of them presents two relatively long intermolecular N···H distances (3.752 and 3.839 Å) with one of the two molecules located in the center of the cell, these distances occur between the nitrogen in position 2 of a pyrazole ring and a hydrogen of the *t*Bu group of the second molecular unit.

For the case of crystal **9b** (Figure 7 middle), the two molecular units in the middle of the cell are located opposite each other forming a centered symmetrical dimer packing. These molecules present two identical N···H distances (3.212 Å) between the nitrogen of a pyridine ring and a hydrogen of the *t*Bu group of the second unit. The other two molecules, located at diametrically opposite vertices, interact with one of the central cell molecules each

through a relatively short HB (2.677 Å), formed between a hydrogen of a pyridine ring of the vertex unit with the nitrogen in position 2 of a pyrazole ring of a central dimer molecule.

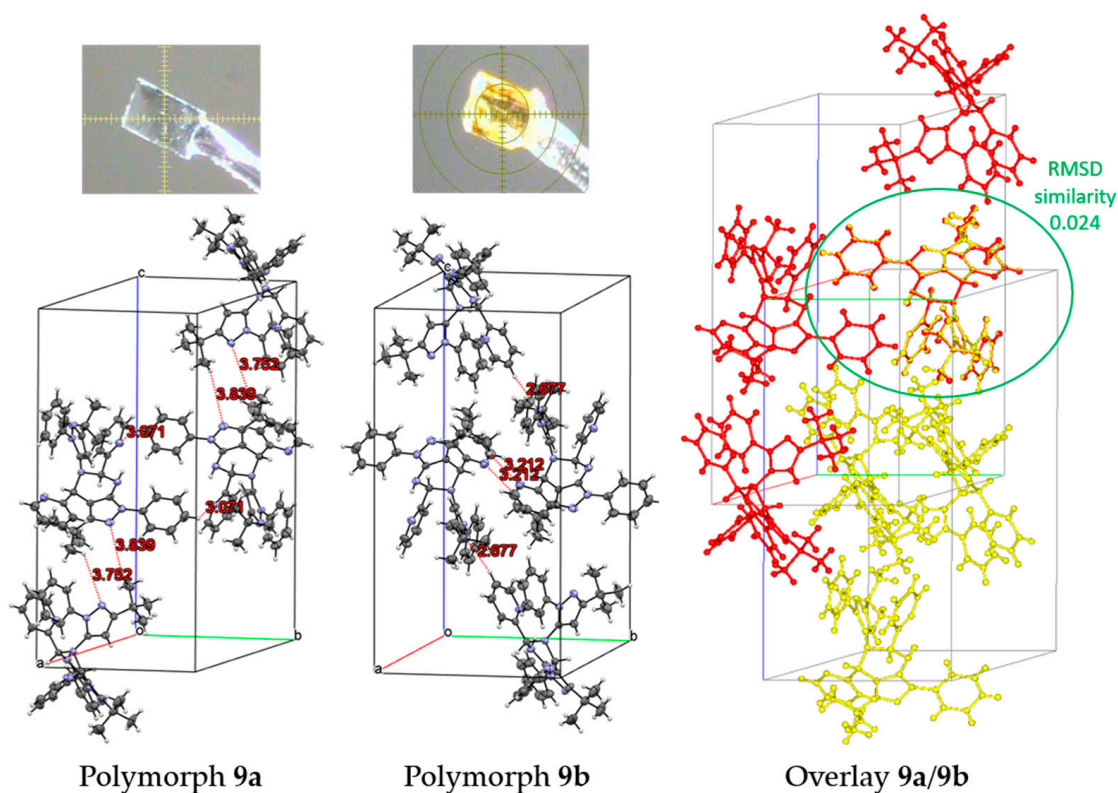


Figure 7. Crystal packing in polymorphs **9a** and **9b** along with the corresponding plot overlay (**9a** in red and **9b** in yellow). Photographs of crystal samples used for X-ray diffractions measurements are included as inserts in this figure.

As shown in Figure 8, the individual molecular units in crystals **9a** and **9b** exhibit a similar three-dimensional conformation, with slight differences between their geometric parameters. In these structures, the central fused pyrazolo-[3,4-*d*]-pyrimidine ring (**A-B** in Figure 2) adopts a distorted-semiplanar configuration, where the functionalized nitrogen (labeled as N5 and N8, respectively) of the pyrimidine (**A** ring) lies out of plane. Coplanarity with the fused **A-B** central ring expands to the **C** phenyl ring; thus favoring the formation of two intramolecular H \cdots N HBs: one (2.453 Å for **9a** and 2.461 Å for **9b**) between an *ortho* hydrogen and the nitrogen (linked to hydrogen) of the pyrimidine (**A** ring), and the second (2.386 Å for **9a** and 2.402 Å for **9b**) between the other *ortho* hydrogen and the unfunctionalized nitrogen of the pyrazole ring (**B**). The amine hydrogen on the pyrimidine forms a short H \cdots N HB (2.277 Å for **9a** and 2.332 Å for **9b**) with the nitrogen of one the pyridine ring **D**, while the unfunctionalized nitrogen on the fused pyrazole (**B**) forms a longer H \cdots N HB (2.554 Å for **9a** and 2.566 Å for **9b**) with one methyl hydrogen of the *t*Bu group linked to the **B** ring. The nonplanar nitrogen (N5 or N8) in the pyrimidine exhibits an H \cdots N interaction (2.524 Å in **9a** and 2.535 Å in **9b**) with one of the *ortho* hydrogens of the phenyl ring **F**, while the same *ortho* hydrogen exhibits a longer H \cdots N distance (2.724 Å in **9a** and 2.730 Å in **9b**) with the nitrogen of the second pyridine (**G** ring). Finally, the unfused pyrazole (**E** ring) presents an H \cdots N HB (2.520 Å in **9a** and 2.522 Å in **9b**) through its unfunctionalized nitrogen with an *ortho* hydrogen of its linked phenyl ring (**F**).

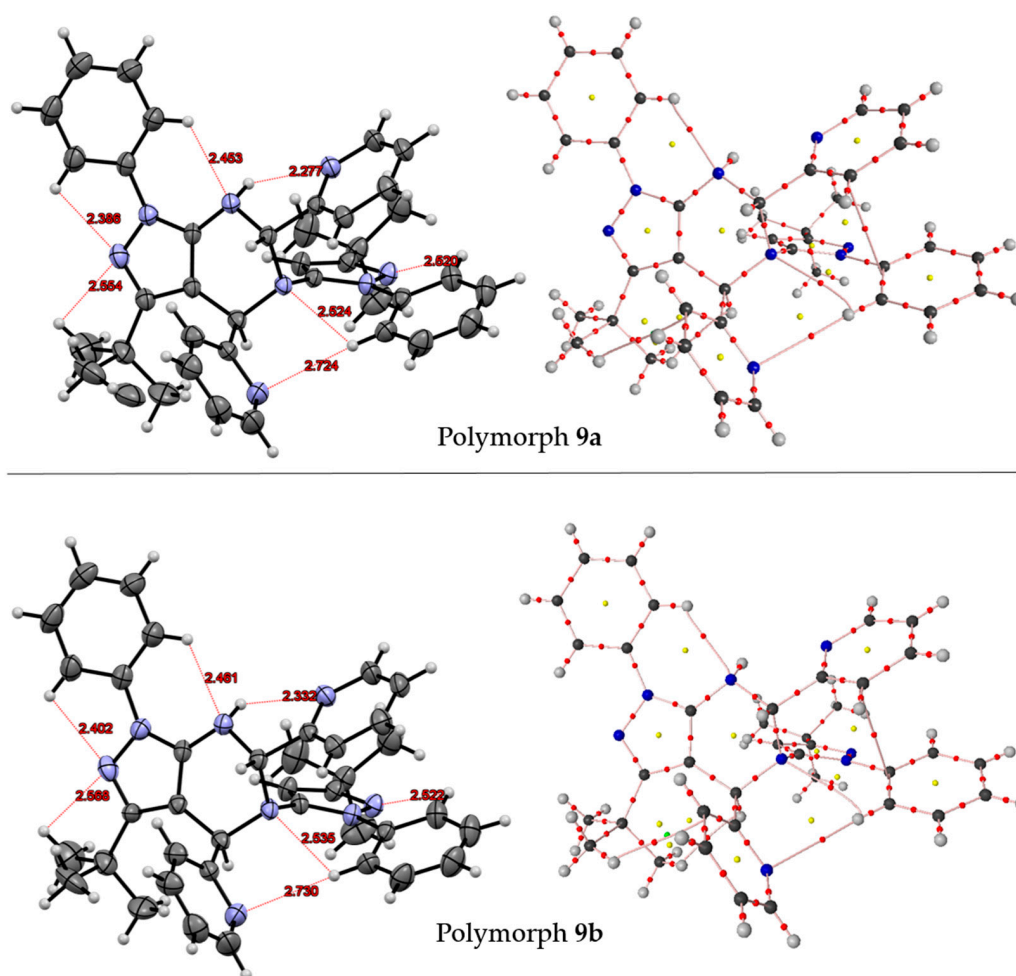


Figure 8. Comparison between molecular units extracted from crystals **9a** and **9b**. (Left) The 3D-ORTEP rendering of the molecular units showing intramolecular HB contacts as red dashed lines with distances in Å. Displacement ellipsoids are drawn with a probability level of 50%. (Right) Molecular graph for molecular units showing bond paths (pink lines), BCPs (red dots), RCPs (yellow dots), and CCPs (green dots).

Analysis of intermolecular interactions in polymorphs **9a** and **9b** revealed a quasi-identical supramolecular architecture between these two crystal packings. As shown in Figure 9, both crystals are characterized by the presence of the same five distinctive close intermolecular interactions, distributed in a $N\cdots H$, two $H_3C\cdots H$, and one bidirectional π stacking $C\cdots H$ HB. $N\cdots H$ HB occurred between the unfunctionalized nitrogen in pyrazole **E** and the hydrogen atom in position 3 of the pyridine ring **D**, with distances of 2.671 and 2.677 Å for polymorphs **9a** and **9b**, respectively. One of the $H_3C\cdots H$ interactions is between the *ortho* hydrogen in phenyl ring **F** and one methyl carbon of the *t*Bu group linked to pyrazole ring **B**, with distances of 2.820 (**9a**) and 2.834 Å (**9b**). The second $H_3C\cdots H$ HB is observed between the hydrogen in position 2 on the pyridine ring **G** and one methyl carbon of the *t*Bu group linked to pyrazole **E**, with distances of 2.877 (**9a**) and 2.891 Å (**9b**). The bidirectional π stacking $C\cdots H$ HB comprises the hydrogen in position 5 in pyridine ring **D** and two geminal carbons in phenyl ring **C**. In crystal **9a**, this bidirectional HB presents distances of 2.834 and 2.888 Å, with angles of 95.8° and 93.9° with respect to the plane of the phenyl ring, respectively. While in crystal **9b**, distances and angles of this bidirectional π stacking contact are 2.837 (95.7°) and 2.892 Å (93.6°). As can be seen when comparing similar noncovalent distances, both intramolecular (Figure 8) and intermolecular (Figure 9), between these two polymorphs, crystal **9a** without exception presents shorter distances; thus denoting a slightly more efficient crystal packing than that of crystal **9b**. Such distance

shortening is therefore reflected in the lower unit cell volume and higher crystal density of polymorph **9a** (Table 1).

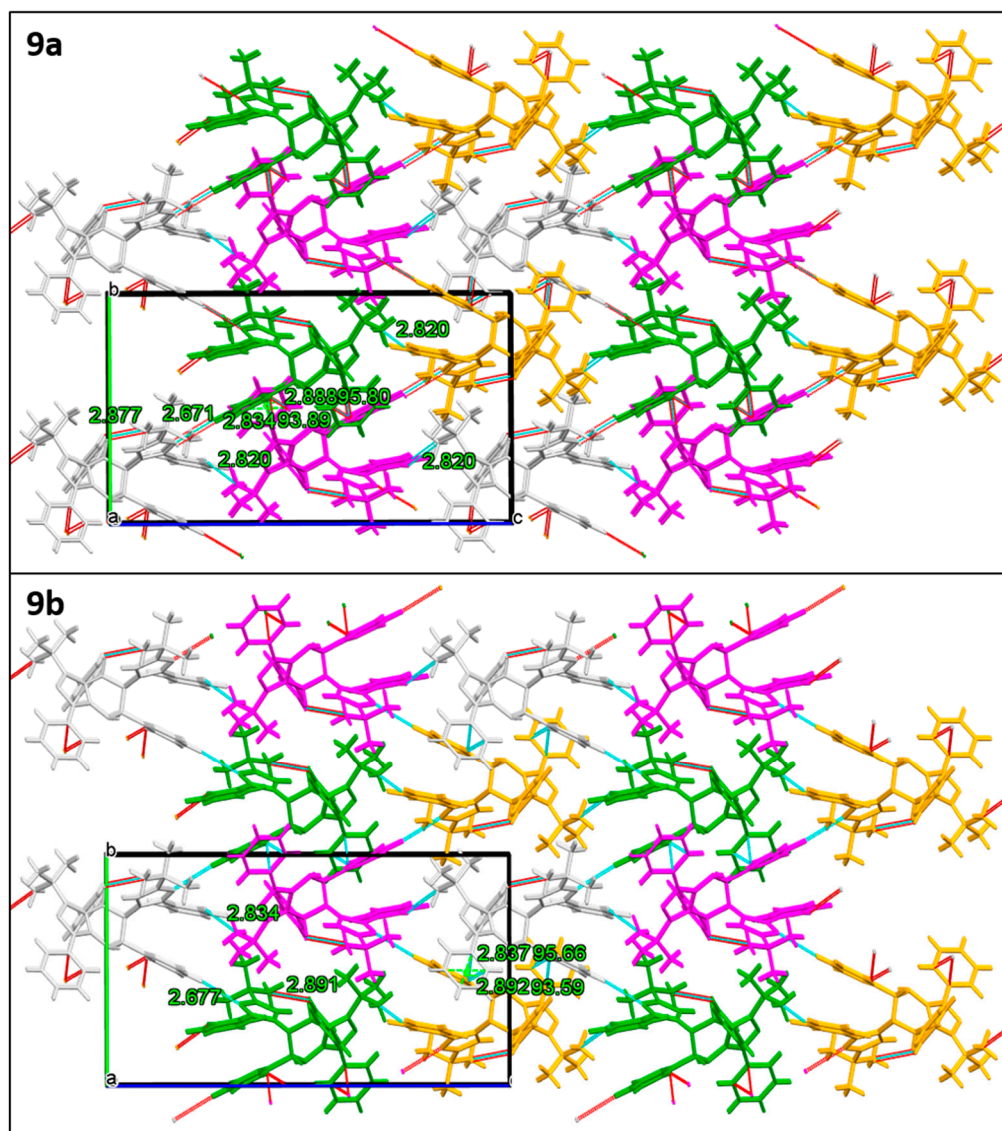


Figure 9. Crystal packing ($2.0 \times 2.0 \times 2.0$ supercell) comparison between the two isostructural polymorphs **9a** and **9b** seen along the bc face and highlighting featured close intermolecular contacts. Molecular units ($Z = 4$, $Z' = 1$) are colored based on different symmetry operations. Distances in Angstroms (\AA) and angles in grades ($^\circ$).

3.2.2. Topological Study on Electron Density (ρ)

The application of QTAIM-C to the gradient field of the electronic density of the crystalline molecules **9a** and **9b** leads to the detection of an equal number of critical points, distributed as 86 NCPs, 98 BCPs, 14 RCPs, and 1CCP. Such a characteristic set satisfies the Poincaré–Hopf relationship ($n \text{ NCP} - n \text{ BCP} + n \text{ RCP} - n \text{ CCP} = 1$), which confirms the completeness of critical points in each of these molecular systems. Molecular graphs for crystalline molecules **9a** and **9b** are presented in Figure 8 (right side). Six closed-shell intramolecular BCs were detected in molecules **9a** and **9b** each, whose main topological parameters are listed in comparative fashion in Table 3. These intramolecular BCPs are associated with three $\text{N}\cdots\text{H}$ bond paths between heterocyclic nitrogen atoms and phenyl hydrogens in *ortho* position, one $\text{C}\cdots\text{C}$ bond path between pyridine **D** carbon and phenyl **F** carbon, one $\text{C}\cdots\text{H}$ bond path between pyridine **G** carbon and a *t*Bu hydrogen, and a $\text{H}\cdots\text{H}$

bond path between pyrimidine **A** hydrogen and a *t*Bu hydrogen. As noticed in Table 3, longer bond paths, along with lesser charge densities, are observed for intramolecular interactions involving *t*Bu hydrogens in crystal molecule **9a** compared to **9b**. As higher ellipticity (ϵ) values are observed in the BCPs for these *t*Bu interactions in crystal molecule **9b**, its slightly higher bond strength could be related to a higher π character than that present in analogous **9a** molecules interactions.

Table 3. Topological parameters¹ (in au) for closed-shell intramolecular BCPs in crystalline molecular units **9a** and **9b**. Ring sorting is presented in parentheses and using bold capital letters as described in Figure 2.

Interaction X...Y	Polymorph	Bond Path		ρ_b	∇_{ρ}^2	ϵ	$V(r)$	$G(r)$
		R_X	R_Y					
H-N(A)...H(<i>ortho</i>)-C(C)	9a	2.7303	1.9148	1.122×10^{-2}	1.091×10^{-2}	2.816×10^{-1}	6.883×10^{-3}	8.898×10^{-3}
	9b	2.7433	1.9108	1.128×10^{-2}	1.108×10^{-2}	3.629×10^{-1}	7.046×10^{-3}	9.061×10^{-3}
N(A)...H(<i>ortho</i>)-C(F)	9a	2.8231	2.0064	1.254×10^{-2}	1.088×10^{-2}	4.211×10^{-1}	7.514×10^{-3}	9.200×10^{-3}
	9b	2.8291	2.0260	1.238×10^{-2}	1.073×10^{-2}	4.436×10^{-1}	7.409×10^{-3}	9.071×10^{-3}
N(G)...H(<i>ortho</i>)-C(F)	9a	3.0917	2.0581	5.960×10^{-3}	4.855×10^{-3}	1.300×10^{-1}	3.088×10^{-3}	3.972×10^{-3}
	9b	3.0989	2.0615	5.888×10^{-3}	4.795×10^{-3}	1.253×10^{-1}	3.045×10^{-3}	3.920×10^{-3}
C(D)...C(F)	9a	3.1648	3.3425	6.218×10^{-3}	4.434×10^{-3}	1.251	2.530×10^{-3}	3.482×10^{-3}
	9b	3.1768	3.3453	6.101×10^{-3}	4.343×10^{-3}	1.223	2.478×10^{-3}	3.410×10^{-3}
C(G)...H-CH ₂	9a	3.5008	2.4909	3.524×10^{-3}	2.612×10^{-3}	4.638×10^{-1}	1.464×10^{-3}	2.038×10^{-3}
	9b	3.4820	2.4468	3.758×10^{-3}	2.777×10^{-3}	5.031×10^{-1}	1.572×10^{-3}	2.174×10^{-3}
H ₂ C-H...H-C(A)	9a	1.9492	1.9951	1.137×10^{-2}	1.096×10^{-2}	1.079×10^{-1}	6.917×10^{-3}	8.942×10^{-3}
	9b	1.9307	1.9772	1.182×10^{-2}	1.141×10^{-2}	1.122×10^{-1}	7.228×10^{-3}	9.320×10^{-3}

¹ Definitions: electron density (ρ_b), Laplacian of electron density (∇_{ρ}^2), ellipticity (ϵ), Virial field function ($V(r)$), Lagrangian kinetic energy ($G(r)$).

3.2.3. Hirshfeld Surface Analysis

Hirshfeld surfaces for crystal polymorphs **9a** and **9b**, mapped onto d_{norm} , curvedness (C), and shape index (S), are presented in comparative fashion in Figure 10. Both HSs exhibit very similar three-dimensional shapes, with slight differences in volume (834.0 Å³ for **9a** and 837.4 Å³ for **9b**) and area (613.8 Å² for **9a** and 614.7 Å² for **9b**); thus revealing a high sharing in type and number of intermolecular interactions occurring among the molecules in each of these crystals.

The darkest red spots in the HS of either of the molecules **9a** and **9b** within the respective crystal are associated with four different types of HB interactions: (i) a reciprocal N...H interaction (2.521 Å for **9a** and 2.528 Å for **9b**) between the unfunctionalized nitrogen on the pyrazole **E** ring and the hydrogen *meta* to nitrogen on the pyridine **D** ring, (ii) a reciprocal π -stacking C...H interaction (2.750 Å for **9a** and 2.753 Å) between an *ortho* carbon on the phenyl **F** ring and an hydrogen of the *t*Bu group linked to the pyrazole **B** ring, (iii) a bidirectional π -stacking C...H interaction between an hydrogen (*meta* to nitrogen) on pyridine **D** ring and two geminal carbon atoms on phenyl **C** ring (2.738 and 2.747 Å for **9a**, 2.742 and 2.752 Å for **9b**), and (iv) a H...C interaction between an *ortho* hydrogen on the phenyl **F** ring and a methyl hydrogen from the *t*Bu group attached to the pyrazole **B** ring (for the case of **9a**) or to the pyrazole **E** ring (for the case of **9b**), with distances of 2.697 and 2.709 Å, respectively.

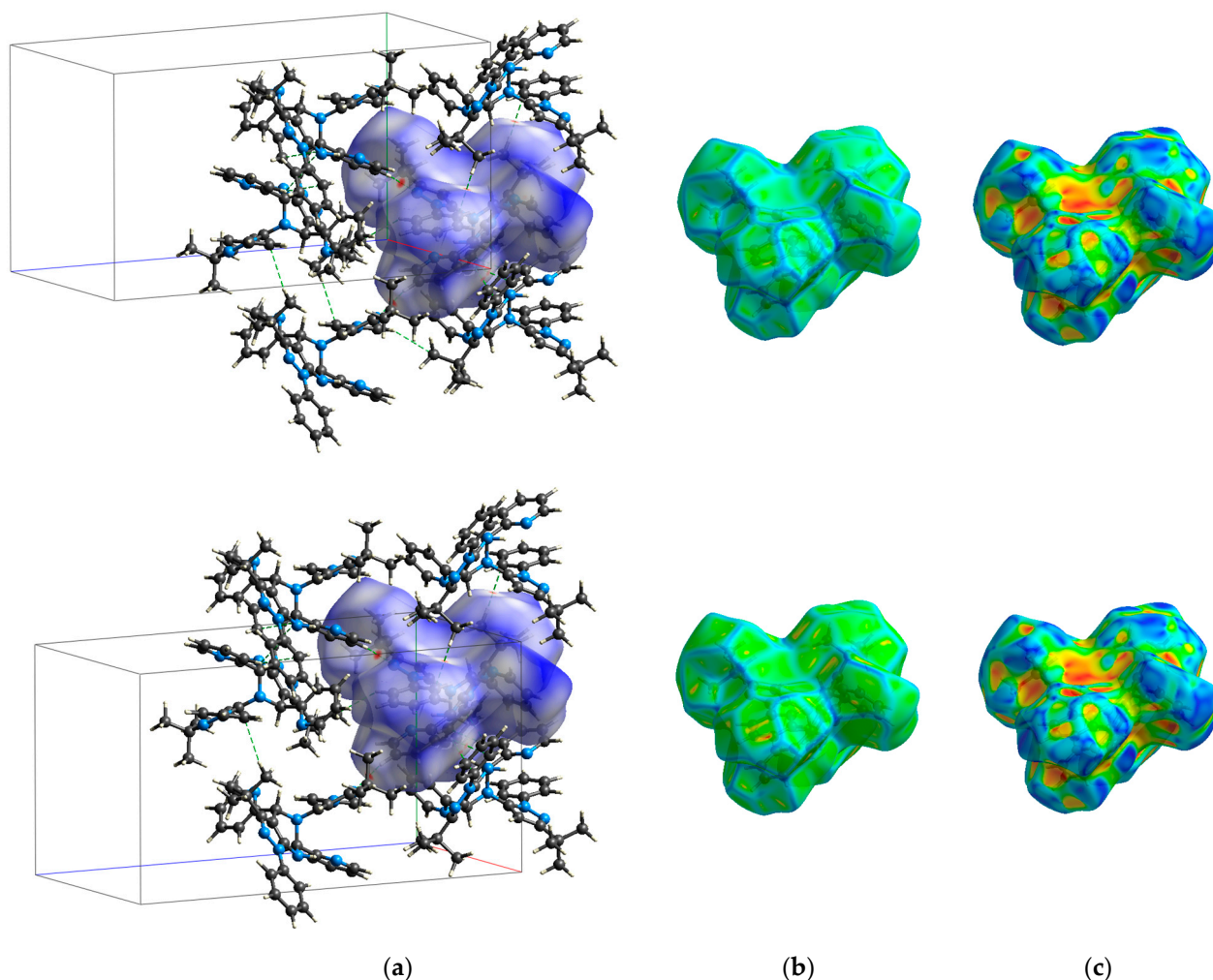


Figure 10. Hirshfeld surfaces (HS) of crystalline molecules **9a** (top row) and **9b** (bottom row) mapped over (a) the normalized contact distance (d_{norm}) scaled over the range -0.08 – 1.54 , (b) curvedness (C) scaled over the range -4.0 – 0.4 , and (c) shape index (S) scaled over the range -1.0 – 1.0 .

Comparison between the 2D-fingerprint plots derived from HSs of polymorphs **9a** and **9b** (Figure 11) clearly highlights the close—almost identical—distribution of intermolecular interactions shared by these crystal structures. In both crystals, $H\cdots H$ interactions prevail with a coverage of 71.0% (**9a**) and 71.1% (**9b**) of the respective HS area. In these FP plots, the small peak centered at $d_e = d_i \cong 1.1$ Å is related to the $H\cdots H$ interaction between an *ortho* hydrogen in phenyl ring **C** and a hydrogen atom of the *t*Bu group linked to pyrazole ring **B**. $C(\text{in})\cdots H(\text{out})$ interactions are the second intermolecular contribution on HS, with only one decimal percentage higher for **9a** (10.9%) than for **9b** (10.8%). The interactions $H(\text{in})\cdots C(\text{out})$, $N(\text{in})\cdots H(\text{out})$, and $H(\text{in})\cdots N(\text{out})$ give the same distribution rate in both HSs in a percentage order descending of 8.9, 4.5, and 4.2%, respectively. The narrow spike at d_e or $d_i \cong 1.1$ Å in decomposed $N\cdots H$ FP plots coincides with the interaction marked as a red spot in HS and denoted as (i). Whereas the rounded edges centered on d_e or $d_i \cong 1.7$ Å in decomposed $C\cdots H$ FP plots correspond to the bidirectional π -stacking $C\cdots H$ interaction marked as red spots in HS and denoted as (iii). In the case of the $C\cdots C$ and $N\cdots C/C\cdots H$ interactions, each of them provides only 0.2% of the interatomic contacts across the HS in **9a** or **9b**.

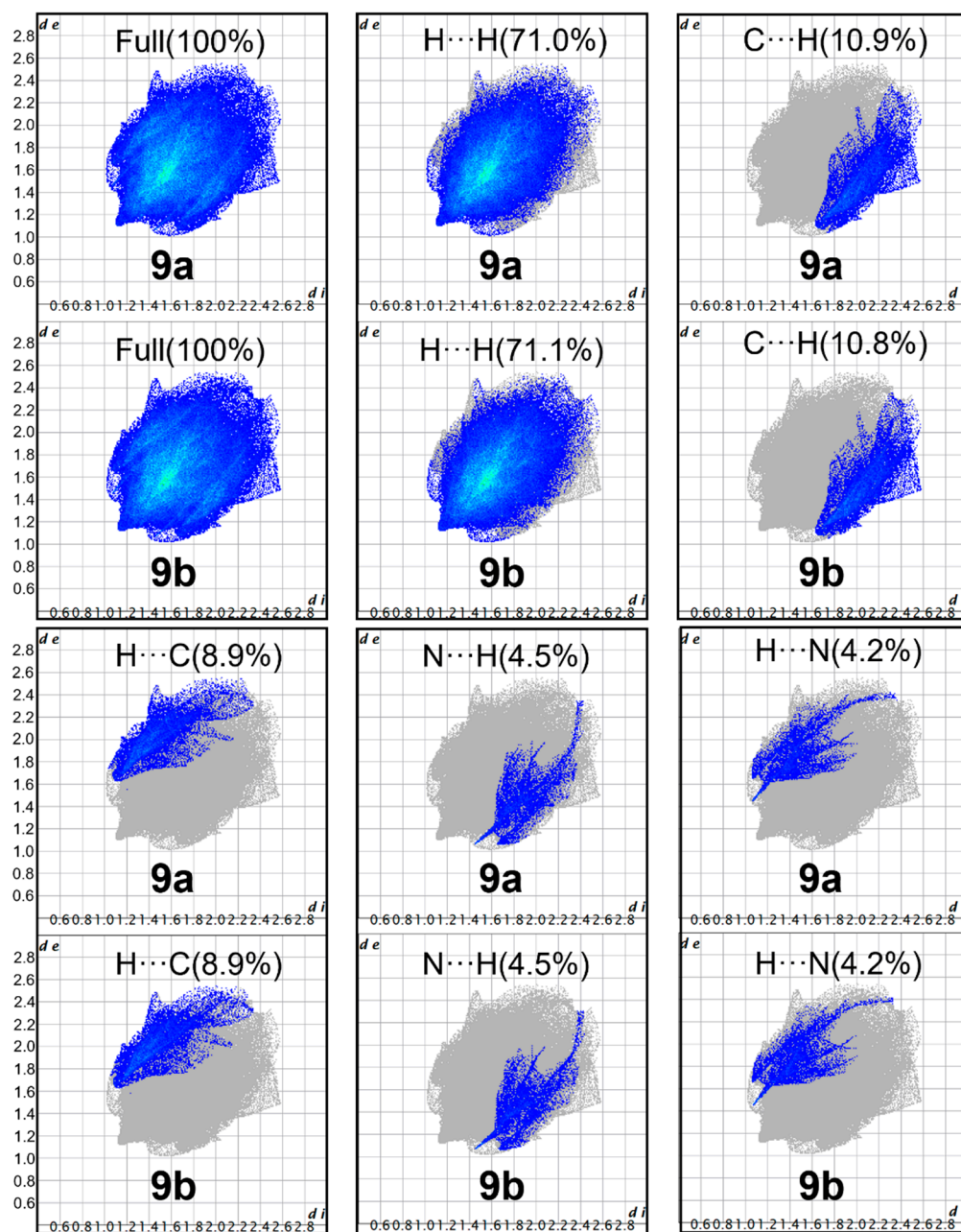


Figure 11. The 2D-fingerprint plots for all and outlined in H···H, C···H, H···C, N···H, and H···N intermolecular contacts through HSs in crystalline molecules **9a** and **9b**. In A···B contacts, atom A is inside HS, while atom B is outside HS.

Empty pores and channels within crystalline structures of polymorphs **9a** and **9b** were also explored by calculating the void surfaces of the unit cells using an isovalue of 0.002 eau^{-3} , as presented in Figure 12. On these surfaces, the boundaries of the empty region are defined by assuming capping faces meeting the walls of the unit cell. The volumes of the voids calculated for crystals **9a** and **9b** were 466.06 and 469.78 \AA^3 , with areas (without including capping faces) of 1383.20 and 1393.35 \AA^2 , respectively. The slightly lower (0.8% smaller) porosity of the crystal **9a** correlates well with the small increase in its calculated density ($\rho = 1.198 \text{ Mg/m}^3$) compared with that of crystal **9b** ($\rho = 1.198 \text{ Mg/m}^3$). The volumes of the voids in crystals **9a** and **9b** occupy 13.8% and 13.9% of the unit cell volume, demonstrating tight packing of the molecules in these crystals at room temperature. Very similar values of void volume (13.6%) were calculated in the molecular crystals of

salicylamide under normal conditions, which could be decreased by as much as 2.0% by increasing the pressure up to 5 GPa [32]. From the void and unit cell volumes of systems **9a** and **9b** (Table 1), volumes of 727.3 and 729.8 Å³ are calculated for each of their molecules, respectively, which agrees with the longest intramolecular distances determined for the **9b** molecule (Section 3.2.1).

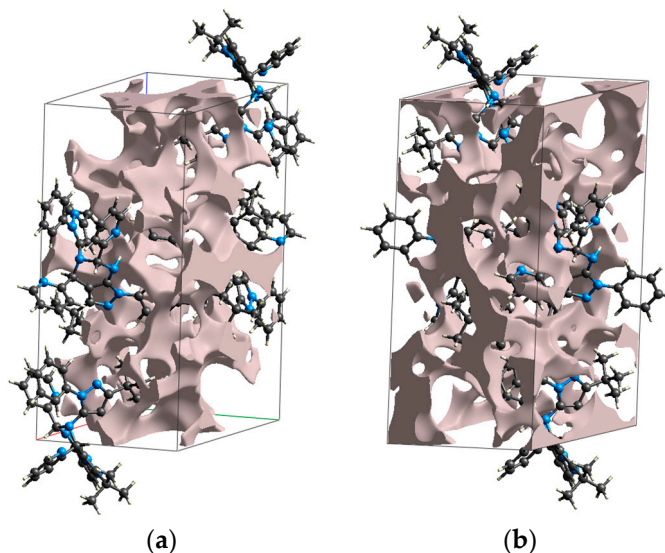


Figure 12. Void surfaces (isovalue 0.002 e.u.⁻³) within the unit cells of crystalline polymorphs **9a** (a) and **9b** (b).

3.2.4. Model Energies and Energy Frameworks

The energies of the interactions between the molecules in crystals **9a** and **9b** were explored using the calibrated energy model CE-B3LYP as implemented in CrystalExplorer [28,33], for which an aggregate of eight molecules located at 3.8 Å around a central molecule was generated in each case. The interaction energy of each pair formed by the central molecule (A) and a cluster molecule (B) is decomposed in terms of electrostatic (E_{ele}), polarization (E_{pol}), dispersion (E_{dis}), and exchange–repulsion (E_{rep}) components, as established in Equation (3).

$$E_{Tot} = k_{ele}E_{ele} + k_{pol}E_{pol} + k_{dis}E_{dis} + k_{rep}E_{rep}, \quad (3)$$

where k_{ele} , k_{pol} , k_{dis} , and k_{rep} are scale factors optimized using B3LYP/6-31G(d,p) monomer wavefunctions (model CE-B3LYP) [28,33].

The molecular clusters used for calculating intermolecular interactions in crystals **9a** and **9b** are presented in Figure 13, while the values of total energy and energy contributions E_{ele} , E_{pol} , E_{dis} , and E_{rep} , for each unique interaction between the central molecule (in yellow mesh) and a molecule of the cluster (in different color) are presented in Table 4. According to what was discussed in previous sections, these molecular clusters share the same type and number of intermolecular interactions, with some variations in their energy magnitudes. A strong interaction of 111.8 (**9a**) and 110.8 (**9b**) kJ/mol occurs between the central molecule and the $-x$, $-y$, $-z$ symmetry-related molecule colored red and blue, respectively. It is between this pair of molecules that mutual bidirectional π -stacking C \cdots H HB occurs between the hydrogen at position 5 on the pyridine ring **D** and two geminal carbons on the phenyl ring **C** (Section 3.2.1). The second largest magnitude interaction, of 39.5 kJ/mol for **9a** and 39.4 kJ/mol for **9b**, occurs with another symmetrically related $-x$, $-y$, $-z$ molecule, colored orange and red, respectively. This pair is characterized by the presence of a significant number of H \cdots H interactions both between the aromatic rings and between the *t*Bu group and the phenyl ring. In all cases, the interaction energy calculated for each unique symmetry-related AB pair was higher for cluster **9a** (Table 4).

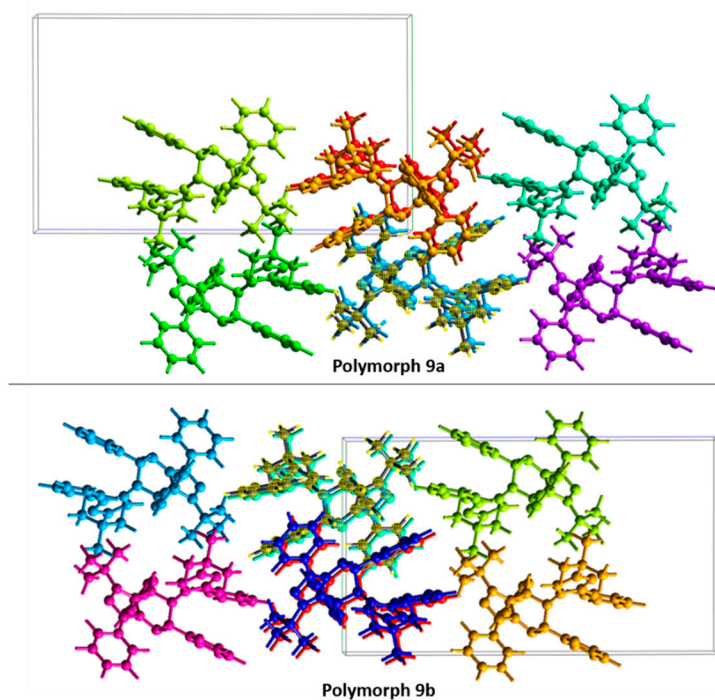


Figure 13. Clusters used for calculating interatomic energies between a unique pair of molecules in crystals **9a** and **9b** with the CE-B3LYP model. The central molecule is highlighted in a yellow mesh and unique symmetry-related molecules are presented in different colors.

Using the same CE-B3LYP model, a lattice energy stability value (ΔE_{Lat}) of 1.2 kJ/mol was estimated for molecular crystal **9a** compared to crystal **9b**, by subtracting the direct sums of the interaction energies of AB pairs [34], as indicated in Equation (4).

$$\Delta E_{Lat} = \frac{1}{2}(E_{Lat \text{ 9a}} - E_{Lat \text{ 9b}}) = \frac{1}{2} \left[\sum_{R(\mathbf{9a})_{AB} < R} E_{tot}^{AB} - \sum_{R(\mathbf{9b})_{AB} < R} E_{tot}^{AB} \right] \quad (4)$$

where E_{lat} converged to a value better than 1 kJ/mol in each case using a summation limit based on the molecular centroid spacing (R_{AB}) of 25 Å.

As shown in Figure 14, a comparison between the energy frameworks for the intermolecular interactions of crystals **9a** and **9b** reveals a cohesive framework of dispersion interactions that overhangs the electrostatic framework. The greatest cohesion by cooperative dispersion effects in these crystals is indicated by the wide green cylinder through the pyrimidine rings between pairs of symmetrically related $-x, -y, -z$ molecules. These pairs are also the ones that provide the greatest stability due to the electrostatic interactions (red tubes) in both crystals. A differential distribution of dispersion energies is found between both systems. On the one hand, crystal **9a** presents strong cohesion through the molecules $-x, -y, -z$ (orange) and x, y, z (light blue) related to symmetry, while in crystal **9b**, this additional contribution is best between the pairs $-x, y + 1/2, -z + 1/2 // x, -y + 1/2, z + 1/2$ (orange // green) and $x, -y + 1/2, z + 1/2 // -x, y + 1/2, -z + 1/2$ (light blue // fuchsia). This behavior occurs exactly in the opposite direction between crystals **9a** and **9b** for the second component of cohesion due to electrostatic effects.

Table 4. Interaction energies (in kJ/mol) for pairs of molecules (AB) in crystals **9a** and **9b** calculated with the CE-B3LYP model. Each color represents a particular interaction between the central molecule and a different symmetry-related molecule.

Color	Polymorph 9a							Polymorph 9b						
	Symop	R_{AB}^1	E_{ele}	E_{pol}	E_{dis}	E_{rep}	E_{tot}^2	Symop	R_{AB}^1	E_{ele}	E_{pol}	E_{dis}	E_{rep}	E_{tot}
Red	$-x, -y, -z$	6.65	-27.2	-6.1	-142.6	73.9	-111.8	$-x, -y, -z$	10.60	-6.5	-1.5	-55.6	27.7	-39.4
Orange	$-x, -y, -z$	10.59	-6.6	-1.5	-56.5	29.0	-39.5	$-x, y + 1/2, -z + 1/2$	15.69	-0.3	-0.1	-4.8	1.5	-3.6
Yellow	$-x, y + 1/2, -z + 1/2$	15.67	-0.3	-0.1	-5.1	1.9	-3.7	$x, -y + 1/2, z + 1/2$	14.61	-1.9	-0.4	-8.9	1.6	-9.1
Light Green	$x, -y + 1/2, z + 1/2$	11.86	-3.1	-0.9	-32.9	15.7	-22.9	-	-	-	-	-	-	-
Green	$-x, y + 1/2, -z + 1/2$	12.64	-12.9	-2.8	-31.8	24.9	-28.0	x, y, z	10.84	-8.0	-1.7	-35.3	18.4	-29.0
Light Blue	x, y, z	10.84	-8.4	-1.7	-35.9	19.2	-29.5	$x, -y + 1/2, z + 1/2$	11.88	-3.1	-0.9	-32.4	15.2	-22.7
Blue	-	-	-	-	-	-	-	$-x, -y, -z$	6.66	-26.9	-5.9	-141.3	72.9	-110.8
Dark Blue	$x, -y + 1/2, z + 1/2$	14.60	-1.9	-0.4	-9.2	1.8	-9.3	-	-	-	-	-	-	-
Purple	-	-	-	-	-	-	-	$-x, y + 1/2, -z + 1/2$	12.65	-12.3	-2.7	-31.1	23.3	-27.7

¹ R_{AB} is the distance (in Å) between molecular centroids (mean atomic position). ² $k_{ele} = 1.057$, $k_{pol} = 0.740$, $k_{disp} = 0.871$, and $k_{rep} = 0.618$.

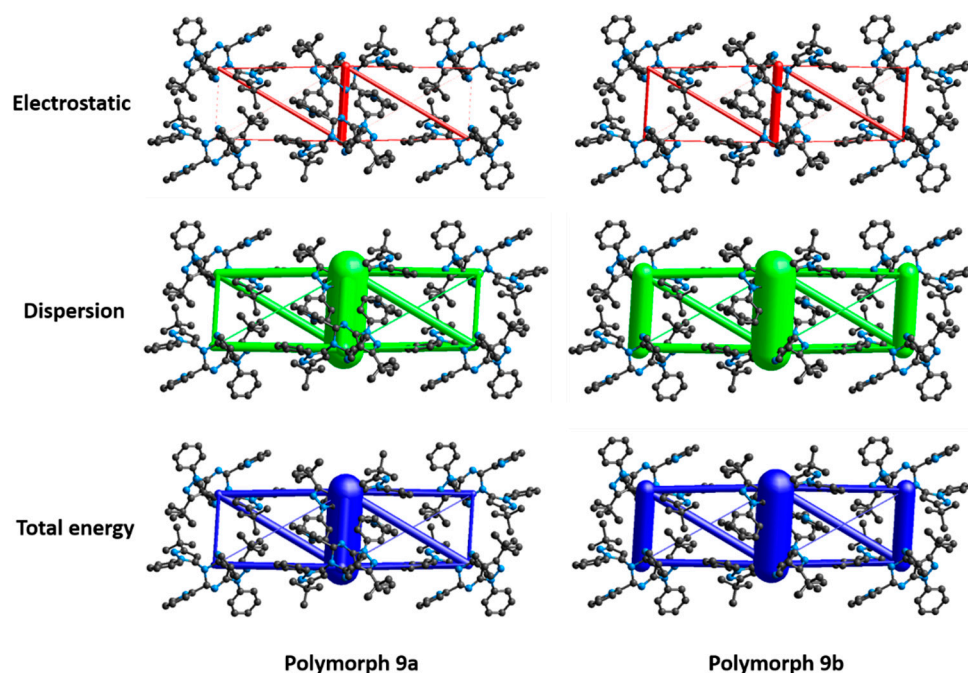


Figure 14. Energy framework diagrams for E_{elec} , E_{dis} , E_{Total} for cluster of molecules in crystalline packing of **9a** and **9b** polymorphs. H atoms have been omitted for clarity and all diagrams used the same cylinder scale of 150 for energies.

4. Conclusions

Two new crystalline derivatives of dipyrazolo-1,5-diazocine and dipyrazolopyrimidine, systems **8** and **9**, respectively, were unexpectedly obtained as products in the reaction of 5-aminopyrazole (**4**) and 2-pyridinecarboxaldehyde (**5**) in ethanol. The original target pyrazole-pyridinemethanamine Schiff base (**6**) is supposed to form in situ during this reaction and evolve to compounds **8** and **9** through two different dimerization processes depending on the addition or not, respectively, of acetic acid as the catalyst. Crystallization of solids **8** and **9** at room temperature using the liquid diffusion technique led to the formation of a single morphological form of **8** and two isostructural polymorphs for **9**, denoted

as **9a** (pale pink crystal) and **9b** (yellow crystal). These latter polymorphs are obtained depending on the solvent treatment used during crystallization. X-ray diffraction studies confirmed without ambiguity the structures for the three molecular crystals, and theoretical/computational studies using Hirshfeld Surfaces (HSs) and topological analysis of the electron density by using the QTAIM enable us to scrutinize the nature and role of the noncovalent interactions in these systems.

In crystal **8**, two molecules pack per cell in a *P*-1 space group system, while short intermolecular H···H interactions (1.984/2.052 Å) between *tert*-butyl groups together with reciprocal π -stacking C···H interactions (2.699 Å) between the *ortho* hydrogen on the phenyl ring and one carbon on the pyridine ring govern its supramolecular constructs. The 2D fingerprint plots reveal an area distribution of approximately 65, 20, and 13% across HS for the intermolecular interactions H···H, C···H, and N···H, respectively. Meanwhile, the application of QTAIM to a molecule extracted from crystal **8** allowed the identification of distinct pairs of C···H, N(Pyridine)···H, and N(Pyridine)···H intramolecular bond paths and the recovery of an unexpected long-range (3.708 Å) intramolecular π -stacking C···H contact between a *tert*-butyl hydrogen and the opposite-located phenyl ring.

Both polymorphs of crystal **9** adopt the same *P*₂₁/*c* packing system with four molecules per unit cell, with slight differences in their cell parameters. The same intermolecular and intramolecular interactions characterized both systems, where crystal **9a** exhibits the shortest contacts leading to a slightly more efficient packing arrangement. The strongest supramolecular interactions in crystals **9a** and **9b** come from the formation of N···H (Py···Py), π -stacking C···H (Ph···*t*-Bu), π -stacking C···H (Ph···Py), and H···C (Ph···*t*-Bu) contacts. The HS analysis allowed the classification of the main intermolecular contributions at approximately 71, 20, and 9% for the H···H, C···H, and N···H contacts, respectively. Quantitative analysis of intermolecular interactions by the CE-B3LYP method revealed a slightly higher supramolecular stability for crystalline assembly **9a**. Both polymorphic structures are mainly stabilized by dispersion interactions, rather than electrostatic hydrogen bond-type interactions.

Supplementary Materials: The following supporting information can be downloaded at: <https://www.mdpi.com/article/10.3390/cryst12050714/s1>, Figure S1: Electron-impact mass fragmentation spectrum of Dipyrazolo-1,5-diazocine derivative (**8**); Figure S2: FTIR spectrum of the dipyrazolo-1,5-diazocine derivative (**8**) measured using the KBr disk technique; Figure S3: ¹H 1D-NMR spectrum of dipyrazolo-1,5-diazocine derivative (**8**) in deuterated chloroform; Figure S4: ¹³C 1D-NMR spectrum of dipyrazolo-1,5-diazocine derivative (**8**) in deuterated chloroform; Figure S5: DEPT NMR spectrum of dipyrazolo-1,5-diazocine derivative (**8**) in deuterated chloroform; Figure S6: The 2D-molecular representation of dipyrazolo-1,5-diazocine derivative (**8**) showing atomic numbering used for NMR assignments; Figure S7: Electron-impact mass fragmentation impact of dipyrazolopyrimidine derivative (**9**); Figure S8: FTIR spectrum of dipyrazolopyrimidine derivative (**9**) measured using the KBr disk technique; Figure S9: ¹H (top) and ¹³C (bottom) 1D-NMR spectra of dipyrazolopyrimidine derivative (**9**) in deuterated chloroform.

Author Contributions: Conceptualization, F.C.-C., R.A. and J.A.G.C.; methodology, F.C.-C. and J.A.G.C.; software, J.A.G.C.; validation, F.C.-C.; formal analysis, F.C.-C. and J.A.G.C.; investigation, F.C.-C. and J.A.G.C.; resources, F.C.-C., R.A. and J.A.G.C.; data curation, F.C.-C. and J.A.G.C.; writing—original draft preparation, F.C.-C., R.A. and J.A.G.C.; writing—review and editing, F.C.-C. and J.A.G.C.; visualization, F.C.-C. and J.A.G.C.; supervision, F.C.-C.; project administration, F.C.-C.; funding acquisition, F.C.-C. and J.A.G.C. All authors have read and agreed to the published version of the manuscript.

Funding: This research was funded by the Universidad del Quindío through the project 1050.

Institutional Review Board Statement: Not applicable.

Informed Consent Statement: Not applicable.

Data Availability Statement: The data presented in this study are available on request from the corresponding author.

Acknowledgments: The authors are grateful to Universidad del Quindío, Universidad del Valle, and Instituto de Química de la Universidad Nacional Autónoma de México (UNAM) for financial support. The authors especially acknowledge Armando Cabrera Ortiz (RIP) from UNAM for his academic assistance and beautiful friendship. J.A.G.C. is especially grateful to the Universidad Pedagógica y Tecnológica de Colombia (UPTC) for the computational facilities provided through the Laboratorio de Química Teórica y Computacional.

Conflicts of Interest: The authors declare no conflict of interest. The funders had no role in the design of the study; in the collection, analyses, or interpretation of data; in the writing of the manuscript, or in the decision to publish the results.

References

1. More, P.G.; Karale, N.N.; Lawand, A.S.; Narang, N.; Patil, R.H. Synthesis and anti-biofilm activity of thiazole Schiff bases. *Med. Chem. Res.* **2014**, *23*, 790–799. [[CrossRef](#)]
2. Borthakur, S.K.; Borthakur, S.; Goswami, D.; Boruah, P.; Kalita, P.K. Synthesis and Antifungal Activities of Some New 5,7-Disubstituted[1,2,4]Triazolo[1,5-a]Pyrimidin-6-one Derivatives. *J. Heterocycl. Chem.* **2016**, *53*, 2079–2083. [[CrossRef](#)]
3. Attaryan, H.S.; Rstakyan, V.I.; Hayotsyan, S.S.; Asratyan, G.V. Non-catalytic Alkylation of Benzylamine with 1,3,5-Trimethyl-1H-pyrazol-4-ylmethanol. *Russ. J. Gen. Chem.* **2013**, *83*, 1178–1179. [[CrossRef](#)]
4. Novikov, M.S.; Khlebnikov, A.F.; Sidorina, E.S.; Masalev, A.E.; Kopf, J.; Kostikov, R.R. 1,3-Dipolar Cycloaddition of Azomethine Ylides Generated from Schiff Bases and Difluorocarbene to Symmetric Olefins. *Russ. J. Org. Chem.* **2002**, *38*, 672–682. [[CrossRef](#)]
5. Chigurupati, S.; Muralidharan, S.; Cin, L.S.; Raser, W.Y.; Santhi, K.; Kesavanarayanan, K.S. Studying Newly Synthesized and Developed 4-Hydroxy-3-Methoxybenzaldehyde Schiff Bases by Uv Spectrophotometry and High Performance Liquid Chromatography. *Pharm. Chem. J.* **2017**, *50*, 851–856. [[CrossRef](#)]
6. Yang, T.; Yu, Q.; Wang, H. Photocatalytic Reduction of CO₂ to CH₃OH Coupling with the Oxidation of Amine to Imine. *Catal. Lett.* **2018**, *148*, 2382–2390. [[CrossRef](#)]
7. Chen, H.; Li, J.; Shen, Z.; Zhou, H.; Hao, L.; Xu, H.; Zhou, X. One-step synthesis of methyl eugenol/Schiff base mesoporous silica nanoparticles sustained-release performance with high lure efficiency. *J. Solgel Sci. Technol.* **2019**, *92*, 723–735. [[CrossRef](#)]
8. Negm, N.A.; Kandile, N.G.; Mohamad, M.A. Characterization and Surface Activity of New Eco-friendly Schiff Bases Vanillin Derived Cationic Surfactants. *J. Surfact. Deterg.* **2011**, *14*, 325–331. [[CrossRef](#)]
9. Feng, C.; Guo, J.-J.; Sun, L.-N.; Zhao, H. Pyrazole Schiff bases cross-linked supramolecules: Structural elucidation and antibacterial activity. *J. Iran. Chem. Soc.* **2018**, *15*, 2871–2876. [[CrossRef](#)]
10. Fernandez, D.; Restrepo-Acevedo, A.; Rocha-Roa, C.; Le Lagadec, R.; Abonia, R.; Zacchino, S.A.; Gómez Castaño, J.A.; Cuenú-Cabezas, F. Synthesis, Structural Characterization, and In Vitro and In Silico Antifungal Evaluation of Azo-Azomethine Pyrazoles (PhN₂(PhOH)CHN(C₃N₂(CH₃)₃)PhR, R = H or NO₂). *Molecules* **2021**, *26*, 7435. [[CrossRef](#)]
11. Moreno-Fuquen, R.; Cuenú, F.; Torres, J.E.; De la Vega, G.; Galarza, E.; Abonia, R.; Kennedy, A.R. Presence of $\pi\cdots\pi$ and C-H $\cdots\pi$ interactions in the new Schiff base 2-((E)-[(3-tert-butyl-1-phenyl-1H-pyrazol-5-yl)imino]methyl)phenol: Experimental and DFT computational studies. *J. Mol. Struct.* **2017**, *1150*, 366–373. [[CrossRef](#)]
12. Cuenú, F.; Londoño-Salazar, J.; Torres, J.E.; Abonia, R.; D’Vries, R.F. Synthesis, Structural Characterization and Theoretical Studies of a new Schiff Base 4-(((3-(tert-Butyl)-(1-phenyl)pyrazol-5-yl)imino)methyl)phenol. *J. Mol. Struct.* **2018**, *1152*, 163–176. [[CrossRef](#)]
13. Cuenú, F.; Restrepo-Acevedo, A.; Murillo, M.I.; Torres, J.E.; Moreno-Fuquen, R.; Abonia, R.; Kennedy, A.R.; Tenorio, J.C.; Lehmann, C.W. Synthesis, structural characterization, and theoretical studies of new pyrazole (E)-2-[[5-(tert-butyl)-1H-pyrazol-3-yl]imino]methyl]phenol and (E)-2-[[1-(4-bromophenyl)-3-(tert-butyl)-1H-pyrazol-5-yl]imino]methyl]phenol. *J. Mol. Struct.* **2019**, *1184*, 59–71. [[CrossRef](#)]
14. Molano, M.F.; Loret, V.P.; Erben, M.F.; Nossa, D.L.; Loaiza, A.E.; Echeverria, G.A.; Piro, O.E.; Tobon, Y.A.; Tayeb, K.B.; Gómez Castaño, J.A. Crystal structure, spectroscopic characterization and Hirshfeld surface analysis of aquadichlorido[N-[(pyridin-2-yl)methylidene]aniline]copper(II)monohydrate. *Acta Cryst.* **2020**, *E76*, 148–154. [[CrossRef](#)]
15. Kumar Jha, K.; Dutta, S.; Kumar, V.; Munshi, P. Isostructural Polymorphs: Qualitative Insights from Energy Frameworks. *CrystEngComm* **2016**, *18*, 8497–8505. [[CrossRef](#)]
16. Dey, D.; Thomas, S.P.; Spackman, M.A.; Chopra, D. ‘Quasi-isostructural polymorphism’ in molecular crystals: Inputs from interaction hierarchy and energy frameworks. *Chem. Commun.* **2016**, *52*, 2141–2144. [[CrossRef](#)] [[PubMed](#)]
17. APEX2; Bruker AXS Inc.: Madison, WI, USA, 2012.
18. SAINT; Bruker AXS Inc.: Madison, WI, USA, 2012.
19. Dolomanov, O.V.; Bourhis, L.J.; Gildea, R.J.; Howard, J.A.K.; Puschmann, H. OLEX2: A complete structure solution, refinement and analysis program. *J. Appl. Crystallogr.* **2009**, *42*, 339–341. [[CrossRef](#)]
20. Sheldrick, G.M. A short history of SHELX. *Acta Crystallogr. Sect. A* **2008**, *64*, 112–122. [[CrossRef](#)]
21. Brandenburg, K.; Putz, H. In diamond, impact, C. In *Crystal Impact*; Kreuzherrenstr: Bonn, Germany, 2006; Volume 102, p. 53227.
22. Macrae, C.F.; Bruno, I.J.; Chisholm, J.A.; Edgington, P.R.; McCabe, P.; Pidcock, E.; Rodriguez-Monge, L.; Taylor, R.; Van De Streek, J.; Wood, P.A. Mercury CSD 2.0 e new features for the visualization and investigation of crystal structures. *J. Appl. Crystallogr.* **2008**, *41*, 466–470. [[CrossRef](#)]

23. Biegler-König, F.; Schönbohm, J. Update of the AIM2000-Program for atoms in molecules. *J. Comput. Chem.* **2002**, *23*, 1489–1494. [[CrossRef](#)]
24. Frisch, M.; Trucks, G.; Schlegel, H.; Scuseria, G.; Robb, M.; Cheeseman, J.; Scalmani, G.; Barone, V.; Mennucci, B.; Petersson, G.A.; et al. *Gaussian 09*; Revision D.01; Gaussian, Inc.: Wallingford, CT, USA, 2013.
25. Bader, R.F. *Atom in Molecules: A Quantum Theory*; Oxford University Press: Oxford, UK, 1990.
26. Spackman, M.A.; Jayatilaka, D. Hirshfeld surface analysis. *CrystEngComm* **2009**, *11*, 19–32. [[CrossRef](#)]
27. McKinnon, J.J.; Jayatilaka, D.; Spackman, M.A. Towards quantitative analysis of intermolecular interactions with Hirshfeld surfaces. *Chem. Commun.* **2007**, 3814–3816. [[CrossRef](#)]
28. Spackman, P.R.; Turner, M.J.; McKinnon, J.J.; Wolff, S.K.; Grimwood, D.J.; Jayatilaka, D.; Spackman, M.A. CrystalExplorer: A program for Hirshfeld surface analysis, visualization and quantitative analysis of molecular crystals. *J. Appl. Cryst.* **2021**, *54*, 3. [[CrossRef](#)] [[PubMed](#)]
29. Kalman, A.; Parkanyi, L.; Argay, G. Classification of the Isostructurality of Organic Molecules in the Crystalline State. *Acta Cryst.* **1993**, *B49*, 1039–1049. [[CrossRef](#)]
30. László, F.; Kalman, A. Volumetric measure of isostructurality. *Acta Cryst.* **1999**, *B55*, 1099–1108. [[CrossRef](#)]
31. Rohlicek, J.; Skorepova, E.; Babor, M.; Cejka, J. CrystalCMP: An easy-to-use tool for fast comparison of molecular packing. *J. Appl. Cryst.* **2016**, *49*, 2172–2183. [[CrossRef](#)]
32. Turner, M.J.; McKinnon, J.J.; Jayatilaka, D.; Spackman, M.A. Visualization and characterization of voids in crystalline materials. *CrystEngComm* **2011**, *13*, 1804–1813. [[CrossRef](#)]
33. Mackenzie, C.F.; Spackman, P.R.; Jayatilaka, D.; Spackman, M.A. CrystalExplorer model energies and energy frameworks: Extension to metal coordination compounds, organic salts, solvates and open-shell systems. *IUCrJ* **2017**, *4*, 575–587. [[CrossRef](#)]
34. Sajesh, T.; Spackman, M.A. The Polymorphs of ROY: A Computational Study of Lattice Energies and Conformational Energy Differences. *Aust. J. Chem.* **2018**, *71*, 279–284. [[CrossRef](#)]